

**SEISMOELECTRIC IMAGING OF A SHALLOW FAULT SYSTEM
EMPLOYING FAULT GUIDED WAVES**

A Thesis

by

FRELYNN JOSEPH REESE COHRS

Submitted to the Office of Graduate Studies of
Texas A&M University
in partial fulfillment of the requirements for the degree of

MASTER OF SCIENCE

May 2012

Major Subject: Geophysics

Seismoelectric Imaging of a Shallow Fault System

Employing Fault Guided Waves

Copyright 2012 Frelynn Joseph Reese Cohrs

**SEISMOELECTRIC IMAGING OF A SHALLOW FAULT SYSTEM
EMPLOYING FAULT GUIDED WAVES**

A Thesis

by

FRELYNN JOSEPH REESE COHRS

Submitted to the Office of Graduate Studies of
Texas A&M University
in partial fulfillment of the requirements for the degree of

MASTER OF SCIENCE

Approved by:

Chair of Committee,	Mark Everett
Committee Members,	Richard Gibson
	Zenon Medina-Cetina
Head of Department,	Rick Giardino

May 2012

Major Subject: Geophysics

ABSTRACT

Seismoelectric Imaging of a Shallow Fault System

Employing Fault Guided Waves. (May 2012)

Frelynn Joseph Reese Cohrs, B.S., Colorado School of Mines

Chair of Advisory Committee: Dr. Mark Everett

Independent sets of reflection seismic and seismoelectric data were collected, processed, and interpreted with the aim of generating and studying guided waves within a fault zone. While seismic surveys have recently been utilized to investigate fault zones, past and current seismoelectric experiments have been more focused on identifying lithological interfaces and the presence of fluids within the shallow subsurface. The utilization of a fault structure to study seismoelectric conversions associated with guided waves has not hitherto been reported in the literature. The purpose of this research is to investigate the capabilities of the seismoelectric geophysical method to image fault structures, and to compare these to the capabilities of the conventional reflection seismic technique. I hypothesize that the presence of subsurface fluids will enhance seismoelectric imaging of a fault system. My results show that seismoelectric data contribute significant new for fault zone characterization and subsurface.

I collected seismic and seismoelectric data sets across a fault system in the Llano Uplift of central Texas. The seismic reflection data were collected with a Geometrics

Strataview seismograph equipped with 36 geophones. The seismoelectric data utilized three Geometrics Geode seismographs, with electric fields recorded by stainless steel dipole pairs instead of geophones. A sledgehammer and an accelerated weight drop provided the seismic energy sources throughout the experiment. Elementary processing techniques were applied to both data sets to enhance the signal to noise ratio.

Seismic reflection studies previously have been shown capable of identifying fault zones through the characterization of guided waves. The seismoelectric phenomenon has not yet been utilized for this purpose. Identification of fault-zone trapped waves within each data set was attempted separately before the two data types were qualitatively compared as to their relative capabilities for illuminating the fault zone. The seismic data revealed dispersive energy packets, indicative of guided waves, within the fault zone and absent in the surrounding lithologies. The seismoelectric data was able to produce comparable signals in the fault zone showing guided waves.

DEDICATION

I dedicate this scientific research to my parents and extended family. Their continued support throughout my higher education career enabled me to persevere for so many years. My future endeavors will undoubtedly benefit from their encouragement.

ACKNOWLEDGEMENTS

I would like to thank my committee chair, Dr. Everett, and my committee members, Dr. Gibson, and Dr. Medina-Cetina for their guidance and support throughout the course of this research.

Very special thanks to Dr. Karl Butler for traveling to Texas, and lending his equipment along with his expertise in collecting and processing seismoelectric data.

I would like to thank Dr. Michael Heaney for introducing me to the field site and assisting with the data collection.

I would like to thank the employees of the Mason Mountain Wildlife Management Area, especially Mark Mitchell, for assistance at the field site.

Thanks also go out to my friends and colleagues within the department who assisted me, including Brandon Bush and Blaine Murphy for help with data collection.

NOMENCLATURE

WMA Wildlife Management Area

LVZ Low Velocity Zone

FZTW Fault Zone Trapped Waves

TABLE OF CONTENTS

	Page
ABSTRACT	iii
DEDICATION	v
ACKNOWLEDGEMENTS	vi
NOMENCLATURE	vii
TABLE OF CONTENTS	viii
LIST OF FIGURES	ix
INTRODUCTION	1
BACKGROUND	3
METHOD	14
SITE DESCRIPTION	16
SEISMIC DATA ANALYSIS	21
SEISMOELECTRIC DATA ANALYSIS	38
DATA COMPARISON AND EVALUATION	50
CONCLUSIONS	53
REFERENCES	55
VITA	57

LIST OF FIGURES

FIGURE	Page
1 Illustration of (EDL) Electric Double Layer (top) and plot of associated electrical potential versus distance from grain surface (bottom)	5
2 Depiction of seismic pressure wave inducing streaming currents through EDL charge separations	7
3 Illustration of (b) interface response, traveling at V_{EM} , created by P-wave interaction at a subsurface material interface	8
4 Illustration of seismoelectric field created by seismic induced pressure wave	10
5 Results of fault-trapped wave numerical modeling	12
6 Entrance to Mason Mountain Wildlife Management Area (WMA)	16
7 Diagram of field site and associated fault contacts	18
8 Photo of the roadcut where the experiment took place	20
9 Fan acquisition geometry of first seismic experiment	22
10 Seismogram record from the second fan-geometry seismic experiment at the Mason WMA field site	23
11 Diagram of second seismic experiment with end-fire acquisition layout	25
12 Seismic line collected in the Hickory Sandstone with 36 channels spaced 3.0 m apart	26
13 Seismogram collected atop proposed fault-zone	26

FIGURE	Page
14 Seismic record for line located within granite at fault zone site	27
15 Overlay plots of seismic traces for the three lithologies tested	29
16 Overlay plots of $f(t^2)$ seismic traces for the three lithologies tested	30
17 Frequency spectrum of the three lithologies, Hickory Sandstone, fault zone, and granite	32
18 Traces from fan geometry and off-end geometry seismic lines, located in fault zone, which cross to tie the collection lines together	34
19 Seismogram of February seismic data collected in fault zone	36
20 Seismic record shot within the granite basement lithology	37
21 Weight drop mechanism mounted to back of vehicle at field site	39
22 Relationships between electrode spacing and coseismic wavelengths recorded	41
23 Side (a) and perspective (b) views of the Lorentz field created by striking a metal plate and hammer for a seismic source	42
24 Map view illustration of the two seismoelectric collection lines overlain atop lithology zones and satellite photo of field site	43
25 Forward shot seismoelectric supergather collected in fault zone	45
26 Reverse shot seismoelectric supergather collected in fault zone	47
27 Reverse shot seismoelectric supergather collected in the granite	47
28 Overlay plots of fault zone trace amplitudes with and without time-squared function applied	48

FIGURE		Page
29	Overlay plots of granite seismoelectric trace amplitudes with and without time-squared function applied	49
30	Three seismic records; (A) Hickory Sandstone, (B) fault zone seismic record, (C) granite seismic record	51
31	Seismoelectric records from Mason WMA field site; (A and B) fault zone, (C) granite area	52

INTRODUCTION

Multiple geophysical methods are currently employed by geoscientists to explore the subsurface and identify geological structures such as lithological boundaries, fault systems, and fluid pathways. While conventional reflection and refraction seismic investigations provide expansive data sets capable of imaging strata at great depths, they should be complemented by alternative data types when possible. Seismoelectric methods have shown excellent imaging capabilities in laboratory and field experiments such that interest in the method has increased over the past twenty years. This non-invasive technique continues to be utilized for a range of applications including contaminant mapping, along with groundwater, mineral, and petroleum exploration activities (Kepic, 1995; Zhu *et al.*, 1999).

The seismoelectric phenomenon relies on seismic to electrical energy conversion in the subsurface. Similar recording units and the familiar variety of acoustical energy sources are used in both seismic and seismoelectric surveys. The primary difference between the two methods, as far as data collection is concerned, is that seismoelectric measurements are carried out using electrode pairs instead of geophones. Interpretation of seismic and seismoelectric data remain similar, although important differences exist.

This thesis follows the style of *Geophysics*.

Past and current seismoelectric experiments have focused on the identification of lithological interfaces and the presence and localization of subsurface fluids (Butler, 1996; Zhu et al., 1999). The characterization of a fault zone structure based on analyzing seismoelectric conversions of a guided wave has not been reported in the literature and it is the primary focus of my research. Detection of a fault-guided wave signature on a seismoelectric record is an important step toward achieving this goal.

I acquired, processed, and interpreted both seismoelectric and seismic data over a known sandstone/granite fault system in the Llano Uplift, Mason County, Texas. I hypothesized that the seismoelectric phenomenon can generate fault-guided wave conversions that are measurable by electrical sensors, and furthermore that an analysis of seismoelectric recordings can provide important insights into the fault zone structure, including its hydrological properties. Conventional seismic data were also recorded to test whether the seismoelectric data provided additional information on the fault structure that was not attainable by the seismic study alone.

BACKGROUND

R.R. Thompson was the first scientist to describe the seismoelectric phenomenon (Thompson, 1936) some 75 years ago. Thompson performed multiple experiments using seismic sources and described the fluctuating electrical currents that result as pressure waves pass through rock volumes. His work was soon followed by contributions from the Russian scientist Ivanov (1939). Ivanov measured an electric field that is confined within and transported by a compressional seismic wave (Haines, 2004). Although research on seismoelectric phenomena continued and progressed after these initial observations, substantive field investigations into the method did not appear until the 1990's.

The past several decades have seen multiple breakthroughs in our understanding of the theoretical basis of seismoelectric phenomena. Russell et al. (1997) identified four distinct effects representing the interaction between seismic and electrical energy: (1) a change in electrical conductivity caused by the fluid pressure changes associated with a seismic wave (Thompson, 1939; Long and Rivers, 1975); (2) piezoelectric effects in quartz grains (Maxwell et al., 1992); (3) electric signals produced through the accumulation of charges on the surface of conductive sulfide bodies (Kepic et al., 1995); and (4) electric signals associated with the motion of electrolytic pore fluid relative to the grain matrix (Haines, 2004). The fourth effect is the most important for the present research. The popular term “electrokinetic” generally describes the conversion of electric

to seismic energy; however, in this research we are considering “seismoelectric”, or seismic to electric, conversions.

The availability of multichannel sensor arrays and high-resolution recording devices, along with the better understanding of seismoelectric phenomena, has propelled theoretical development since the 1980's. Quantitative work by Neev and Yeatts (1989) and later experimental research by Thompson and Gist (1993) has helped to advance seismoelectric research to its present state. Crucial seismoelectric theory published by Haartsen and Pride (1997) delivered a comprehensive understanding of seismoelectric phenomena for fluid-saturated materials by unifying Biot's poroelastic theory (Biot, 1956a,b) with Maxwell's electromagnetic equations. Haartsen and Pride's theory enabled other researchers to validate their interpretation of field observations. Researchers such as Wolfe, Beamish, Butler, and Haines have now established the method for near-surface applications by providing extensive field study and numerical modeling results.

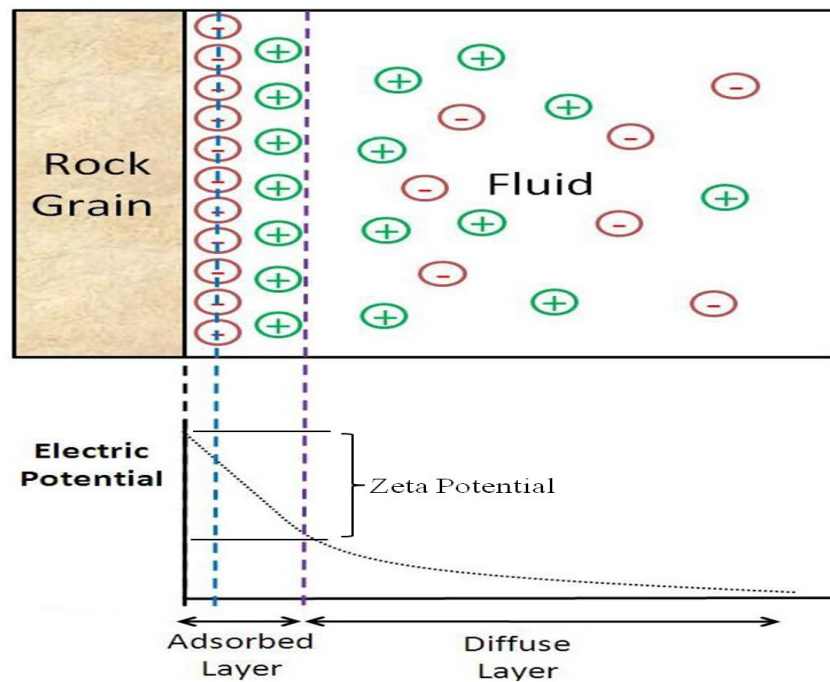


Figure 1. Illustration of (EDL) Electric Double Layer (top) and plot of associated electrical potential versus distance from grain surface (bottom). The electric double layer is comprised of an adsorbed layer and a diffuse layer. The first layer, or bound layer, is a sheet of immobile charges. The diffuse layer contains mobile charged ions. The separation of charges in this second layer, measured as zeta, relative to their location to the grain surface enables seismoelectric conversion, after Gorham (2010).

The seismoelectric method depends upon a micro-scale interaction of grain surfaces with the pore fluids that have been set in motion by seismically-induced fluid pressure gradients. During the 1950's, Biot theorized that a small relative motion occurs between the pore fluid and grain surfaces when a seismic wave energizes a partially-saturated porous medium (Biot, 1956a,b). These small motions are affected by the “electric double layer” which resides in natural porous materials that are variably or completely saturated with electrolytic fluid. The electric double layer (EDL) comprises a

layer of ions adsorbed on a mineral surface and a mobile layer of counterions extending into the liquid phase (Biot, 1956a,b). The electric zeta potential, ζ , between the grain surface and interior of the fluid is a measure of the amount of adsorbed charge. Figure 1 illustrates the electric double layer (EDL) and the ζ potential (Gorham, 2010).

A propagating seismic wave causes the fluid pressure in the pore space to oscillate in concert with the compression and dilation of the solid matrix. Positive and negative ions are advected with the fluid. A charge imbalance thus develops due to the difference in electrolytic mobilities between the positive and negative ions; some of the positive ions, for example, experience a drag caused by the presence of the adsorbed charge layer. A streaming current that arises is associated with the discharge of the charge imbalance in the conductive pore fluid. The streaming current, in turn, is the source that generates the observed seismoelectric signal. Pride and Haartsen derived and published the governing equations for seismoelectric phenomena conversions based on the mechanism just described (Pride, 1994; Pride and Haartsen, 1996; Haartsen and Pride, 1997).

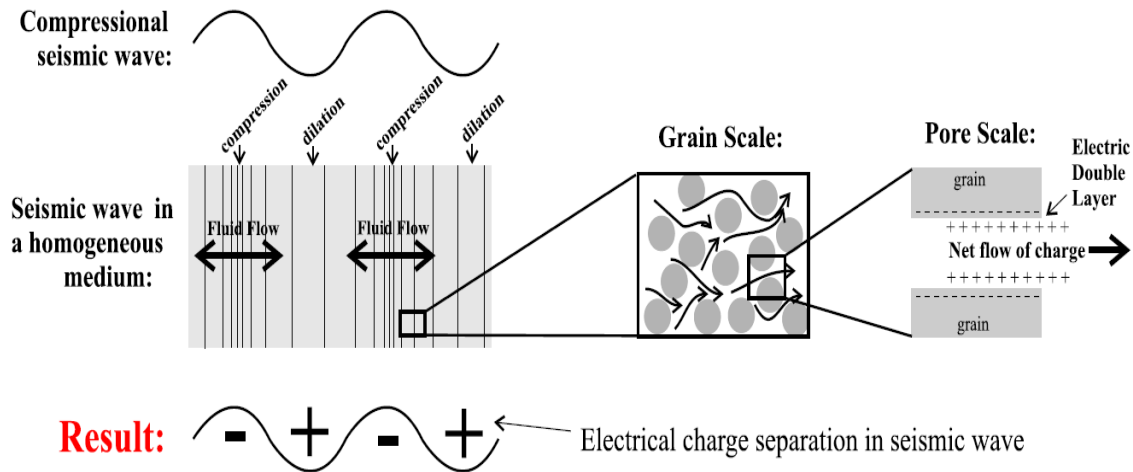


Figure 2. Depiction of seismic pressure wave inducing streaming currents through EDL charge separations. From left to right, a seismic wave is broken down into repeating regions of compression and dilation, grain matrix and associated pore throats are shown to exist inside of the differing regions of the seismic wave, the electric double layer is described as existing between the grain surfaces and containing a net flow of charge. The combination of the electric double layer in between the grains and the therefore inside one of two regions of the seismic wave results in streaming currents. Seismoelectric phenomena rely upon these streaming currents. (Haines, 2004)

At least three seismoelectric fields may be generated and possibly measured in a field survey. The first, and most studied, is the “coseismic” field that is generated as a seismic wave causes pressure-induced fluid motions. As described above, the resulting charge mobilization generates a charge imbalance that is offset by an equal and opposite electric “streaming” current. The seismoelectric conversion is located within the zones of expansion and contraction of a compressional (*P*) wave; it is the most commonly observed seismoelectric phenomenon (Haines, 2004). An illustration of the coseismic field is presented in Figure 2.

The second seismoelectric effect is the “interface response” that is generated when a P wave is incident upon a material interface characterized by differences in material properties (chemical or physical). As the downward-propagating seismic wave is disrupted, a virtual disk of small oscillating electric dipoles forms within the first Fresnel zone (Thompson and Gist, 1993). The Fresnel zone is the cross-section of a volume of an interface or obstacle in the path of propagating waves. The resulting seismoelectric interfacial signal propagates upward at electromagnetic wave velocities that are several orders of magnitude faster than corresponding seismic velocities ($V_{EM} \approx 10^5 V_P$). The interface response can be utilized to locate the water table and resolve thin-beds since it is generated by subsurface discontinuities (Haines, 2004). Figure 3 shows a representation of the “interface response”.

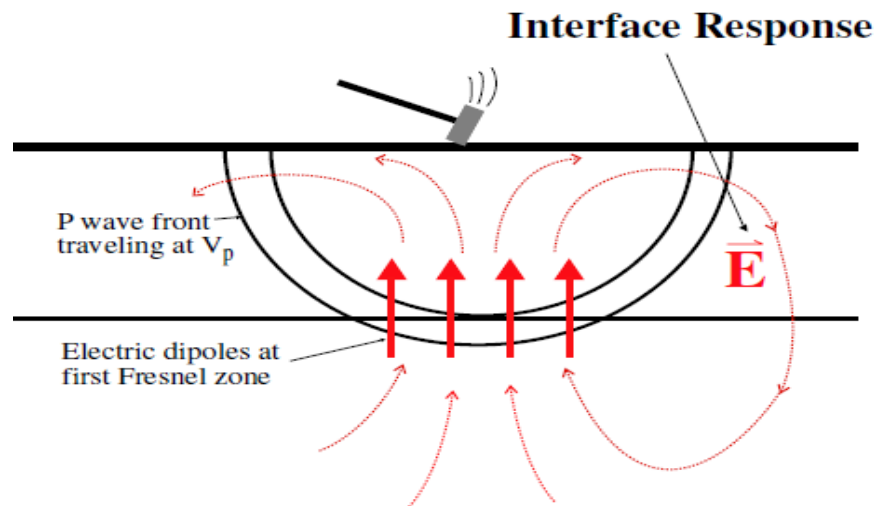


Figure 3. Illustration of (b) the interface response, traveling at V_{EM} , created by P-wave interaction at a subsurface material interface. (Haines, 2004)

The final seismoelectric effect to be considered, termed the “direct field” by Haines (2004), is generated when a seismic point source, such as a sledgehammer blow, creates ground deformation and accompanying fluid-pressure gradients in the immediate vicinity of the impact point (see Figure 4). Sudden elevation of fluid pressure introduced to one side of the impact point and decreased pressure on the opposing side sets up a charge separation as the ground equilibrates and rebounds. The charge separation behaves as a strong oscillating vertical dipole that radiates an electromagnetic field from the impact location. The associated electric field to be generated and measured is termed the direct field. This direct field travels with electromagnetic velocities similar to those of the interfacial response. It is observed within the first portion of a seismoelectric record, analogous to a seismic direct wave. While the direct field is often observed on field electrograms, the main focus of current seismoelectric field experiments involves the analysis of coseismic and interface responses since these are most sensitive to subsurface properties. As is such, the direct field will not be investigated in the seismoelectric shot records.

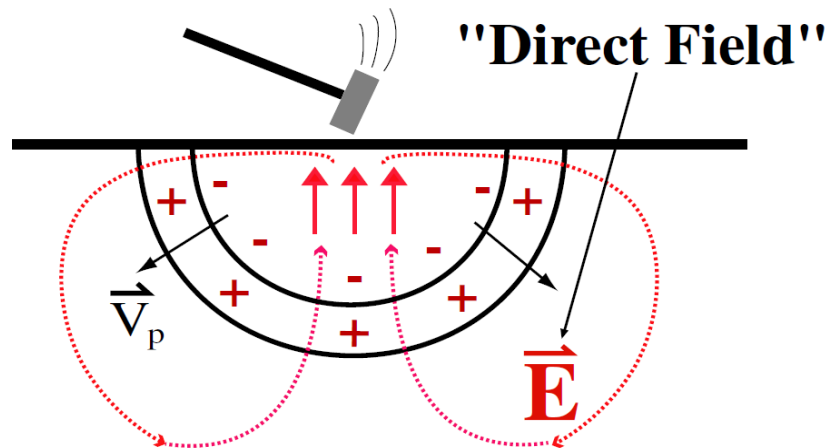


Figure 4. Illustration of seismoelectric field created by seismic induced pressure wave. The passing pressure wave induces asymmetrical charge distribution which acts as an oscillating electric dipole. (Haines, 2004)

Traditionally, seismoelectric surveys have been performed with compact sources such as a sledgehammer or shotgun, along with an electrode array, and a modified seismograph. The seismograph is normally used in conjunction with preamplifiers for enhancing the signal to noise ratio. Custom-made preamplifiers have been utilized in past experiments (Butler, 1996). Alternating geophone and electrode sensors connected to a seismic cable can be used to simultaneously record seismic and seismoelectrical responses or the surveys can also be collected independently. Explosives (Haines, 2004) and vibroseis equipment (Gorham, 2010) have been used in several field surveys. Once seismoelectric data are collected, a number of specific processing techniques should be applied prior to interpretation (Butler and Russell, 1993).

Seismoelectric signals that originate from seismic waves trapped in low-velocity fault zones (LVZ) have not yet been reported in the literature. Fault-zone trapped seismic waves (FZTW) have been recently modeled and studied for purposes of fault-zone structure characterization and earthquake rupture mechanism investigations (Li and Vidale, 1996). FZTW have slow seismic velocity, generally arriving after head and direct waves, and are associated with multiple critically-reflected or post-critically-reflected phases (Ben-Zion, 1998). The trapped S-waves are analogous to Love waves while the trapped P-waves are analogous to Rayleigh waves. Trapped fault waves are recognized in field seismograms as late-arriving large-amplitude dispersive packets. Seismologists have only recently considered FZTW analysis as a method for improved fault zone identification (Ben-Zion, 1998). Surface waves are not directly considered in this study, a simplifying assumption that has also been made in other experiments (Mikhailoz, Haartsen, and Toksov, 1997), even though it is known that surface waves contribute significantly to the overall trapped wave energy (Wu and Hole, 2011).

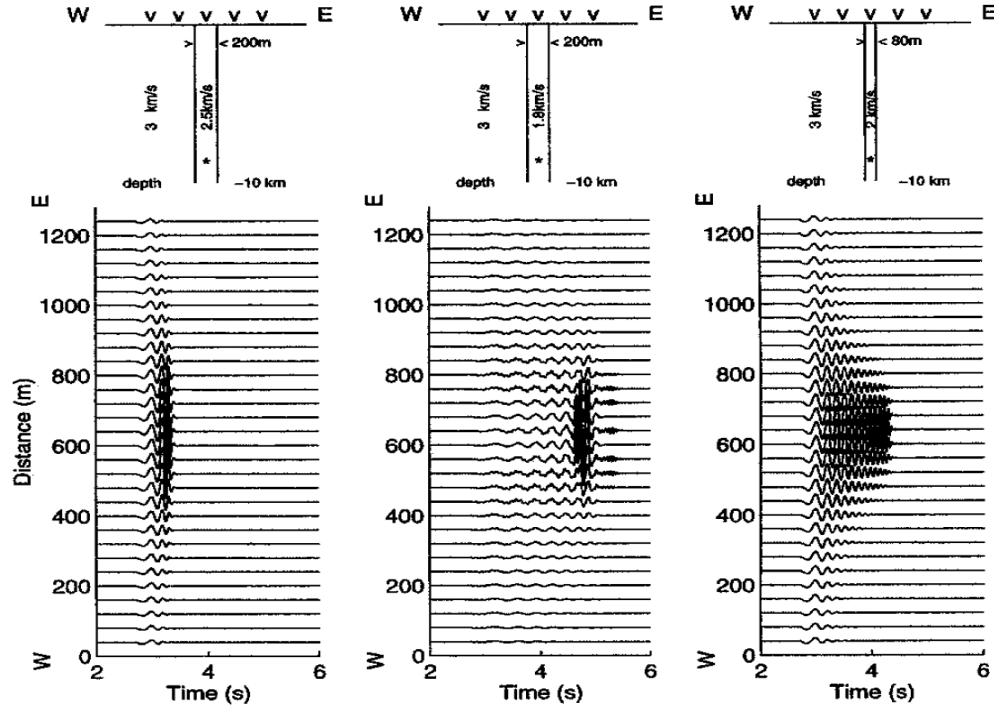


Figure 5. Results of fault-trapped wave numerical modeling. Three plots show the effect of varying fault-zone width and velocity contrast. (Li and Vidale, 1996)

Extensive finite-difference simulations and numerical modeling has enabled predictions of fault-trapped wave behavior (Li and Vidale, 1996). It was found that locating the seismic energy source within the fault zone excites most efficiently the guided waves. Maximum seismogram amplitudes are recorded across the fault plane if the energy source is located exactly on the boundary of the fault zone. Sources directly centered within the fault zone radiate less high-frequency trapped energy. Furthermore, dispersion of guided waves is controlled by the velocity contrast of the fault zone relative to the surrounding, generally higher-velocity lithologies. This effect can be seen in Figure 5 which shows the change in amplitude and dispersion pattern as the fault-zone

width and velocity contrast is altered. An increased contrast in the velocity profile, across a fault zone, results in a more dispersed guided wave signal. Another modeling prediction is that the width of the low-velocity fault zone controls the frequency content of the trapped waves. Lastly, the modeling has shown that fault-zone guided waves are stronger and more distinctive if the fault zone outcrops at the surface, i.e. there is no overburden (Li and Vidale, 1996).

METHOD

Due to the fact that guided waves energized by the seismoelectric phenomenon are rarely used to characterize fault zones, a well-understood geophysical method is needed for calibration. Conventional seismic data collected at the field site serves this purpose and provides comparative information and results. Identification and characterization of trapped waves, attributed to the fault zone, based on seismic shot records was performed before the seismoelectric data were collected and analyzed.

The likelihood of observing fault-guided waves in seismic or seismoelectric records can be enhanced by two factors. The first is the establishment of favorable field acquisition geometry. This can be accomplished in a trial-and-error fashion by deploying the seismic source, sledgehammer, and/or accelerated weight drop, in different locations relative to the fault plane. The strongest guided wave, within the fault, should occur when the energy source is placed directly upon the fault plane. In our experiment, seismic data were acquired within from separate lines within the fault zone and within the associated hanging and footwalls. Seismic data were also acquired along an arc crossing the fault zone to examine the lateral changes in seismic response across the three lithologies. The second factor relevant to identifying guided waves on a seismic or seismoelectric record is the data processing. For example, pre-amplifying seismoelectric signals is crucial to the recognition of small-amplitude, low-frequency wave arrivals. Data filtering and stacking are also performed to remove ambient noise.

Comparing the collected seismic and seismoelectric data sets will involve separately identifying fault-trapped waves on each type of record. Once the signals have been identified on the independent records, normally as late-arriving dispersive wave packets, they are qualitatively compared. First, the ability of the methods to simply detect a fault-trapped wave train is assessed. Conventional seismic experiments have been shown to be capable of detecting fault-guided waves. Whether the seismoelectric method is able to image fault zones with fault-trapped P-waves and coseismic signal conversion is the essential objective of this research.

SITE DESCRIPTION

The test site selected for this research is located in the Mason Mountain Wildlife Management Area (WMA), Figure 6, near Mason, TX. The regional geology of the field site is well known as the area has been studied for many years by Texas A&M students and is utilized as a field laboratory for undergraduate courses. Employees of the WMA allow students to stay in a designated lodge on site to study for extended periods of time.



Figure 6. Entrance to Mason Mountain Wildlife Management Area (WMA), Mason County, Texas, USA

The following is a brief description of the Mason Mountain WMA taken from the website www.tpwd.state.tx.us/huntwild/hunt/wma/find_a_wma/list/?id=14, accessed March 2012:

Located in the Llano Uplift, Mason Mountain Wildlife Management Area was a working exotic game ranch before Texas Parks and Wildlife Department acquired the tract in 1997. Today, 14 species of resident exotics provide excellent opportunities to study the effects of African ungulates on local habitat, and interactions between exotic and native wildlife. The resources of Mason Mountain WMA are dedicated to research concerning the ecology of the Central Mineral Region, and its application to wildlife management on private lands.

The Area is situated on the boundary between the Central Mineral Region and the Edwards Plateau, and as such, a variety of wildlife habitats are represented. About two-thirds of the Area consists of granite derived soils supporting a community of post oak and blackjack oak. The remainder of the Area is dominated by live oak and Texas oak on limestone derived soils. The topography of the Area is rough, with steep canyons, caliche hills, and granite outcrops. An 8-foot fence to facilitate scientific investigations encloses the Area. In order to properly manage the habitat, deer populations are maintained at approximately one deer to 12-15 acres, substantively lower than much of the Hill Country.

The Llano Uplift in the central Texas Hill Country is a circular geologic dome of mainly Precambrian granite that likely formed in association with the Mesoproterozoic Grenville orogeny. Four Cambrian units are of interest: listed by increasing age they are the Point Peak Siltstone, Morgan Creek Limestone, Cap Mountain Sandstone, and Hickory Sandstone. These units overlie the Precambrian crystalline rock. The Llano Uplift shapes the landscape of the Central Texas Hill Country and is rimmed by lower Paleozoic rocks typically covered by regional Cretaceous limestones. Tectonic movements during the Pennsylvanian period produced high-angle faults trending NE-

SW. Fault displacements of up to several km along with erosion especially during the Triassic period has produced the present-day fault structure.

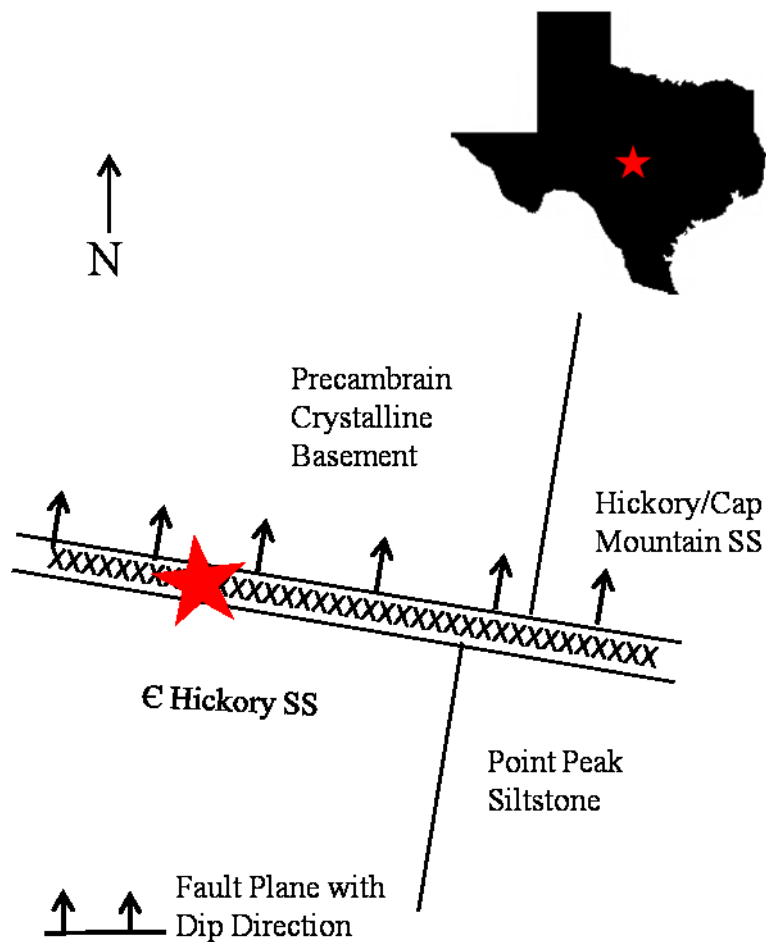


Figure 7. Diagram of field site and associated fault contacts. Red star indicates position of experiment relative to surrounding lithologies.

The field site is situated atop a high-angle, near-vertical normal fault that juxtaposes dry Hickory Sandstone and Precambrian crystalline basement rocks. The fault strikes East 10° South (Figure 7). A road running East 25 ° North was used a reference azimuth from which the strike of the fault was reckoned during the multiple trips to the site. The Hickory Sandstone grades upward from basal fluvial braided stream sediment into shallow marine deposits. It is subdivided into three distinct units: the Upper, Middle, and Lower Hickory. The latter, the only Hickory unit occurring at the field site, varies in color from bright red to deep maroon and is composed of moderately sorted, rounded quartz grains. Only the Lower Hickory is seen at this field site. The underlying Precambrian crystalline basement rock is pegmatitic granite, orange-pink in color. Due to millions of years of weathering, erosional, and soil-forming processes, there remain limited surface outcrops of these lithologies. We therefore relied upon examination of a road cut, Figure 8, to identify the fault strike and dip by locating the zone of contact between the sandstone and granite units. Identification of the fault zone throughout the test site area was carried out by mapping changes in sediment color and composition on the surface. The width of the proposed fault zone was found to be ~25 m. A more precise fault width may be determined from interpretation of the seismic data.



Figure 8. Photo of the road cut where the experiment took place.

This field site fits the needs of this experiment in several ways. Firstly, the site is located within relatively easy driving distance ~500 km west of College Station, TX. We were allowed open access to the area on multiple occasions and were able to drive vehicles directly to the fault zone. There is little surface vegetation, allowing for better propagation and recording of the guided waves. High levels of rainfall in the area during the months preceding the seismoelectric acquisition, may have also positively contributed to the experiment since the seismoelectric conversions depend upon the presence of subsurface pore fluids.

SEISMIC DATA ANALYSIS

Although the novel aspect of this research is based upon analysis of seismoelectric conversions, seismic data sets were also collected to serve as an important baseline for comparison to the seismoelectric data sets.

A total of thirteen seismic records were collected during fall and winter, 2011. All seismic data were collected using a Geometrics Strataview seismograph equipped with vertical-motion 14 Hz geophones. Data were recorded on the seismograph's built-in hard drive and, as needed, seismographs were printed in the field.

The first reflection seismic data set was collected in November 2011. Two seismic lines were laid out in a fan geometry spanning what was believed to be the fault zone. This geometry involves laying out the geophone cable in a circular arc with the shot point at the center such that each shot-geophone distance is equal to the radius of the arc. The shot point is located roughly in the center of the fault zone. The fan geometry of the receivers enables the shot records to be interpreted without having to correct the travel times for variable shot-geophone distances, i.e. there is no trace-to-trace moveout. The acquisition layout shown in Figure 9, with the source located directly atop the fault plane, is intended to probe the lateral extent of a fault zone by the excitation of trapped waves. This particular layout is sensitive to FZTW since seismic signals are acquired from raypaths that travel completely within, partially within, and completely outside the fault zone.

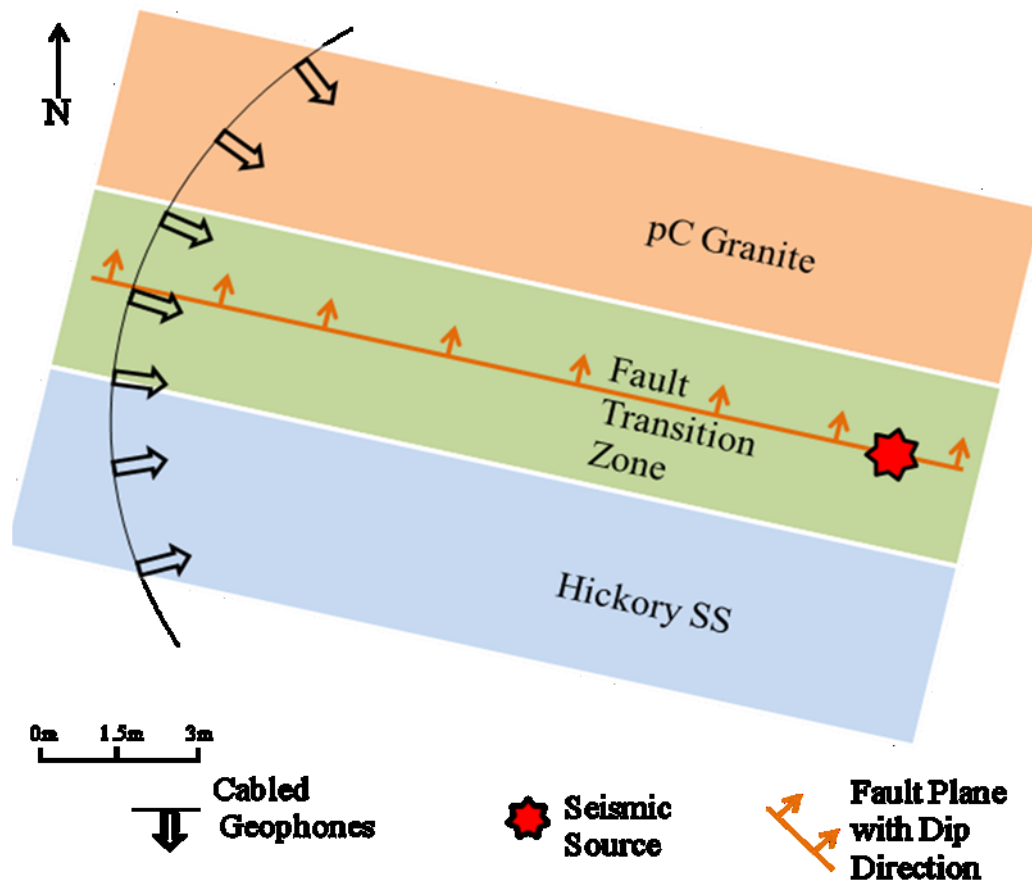


Figure 9. Fan acquisition geometry of first seismic experiment. Placement of geophones relative to seismic source and fault is to enhance identification of the fault zone without geometrical spreading and move out of recorded signals.

The seismic line utilized 36 geophones spaced at 1.0 m intervals with the shot point located 30 m from each geophone in the fan. A record of 128 ms duration was collected at a 125 μ s sampling rate. A 10 ms pre-trigger delay was recorded, and used as the default trigger delay on the remaining seismic line experiments. The stacked ($N=9$) shot record from the first seismic line revealed very little evidence for fault-trapped waves. Investigation of the surface geology in the area concluded that the lateral

transition zone between the sandstone and granite formations is wider than originally thought and that shotpoint was not optimally placed within that zone. A second fan experiment with a larger radius and translated center was then conducted to increase the possibility of resolving the fault zone.

The second seismic fan layout was shifted 35 m to the north of the first layout with increased radius, using 36 geophones spaced at 3.0 m. The shotpoint was again placed in the center of the fault zone. This longer line was recorded twice with record lengths of 256 and 512 ms at respective 250 and 512 μ s sampling rates.

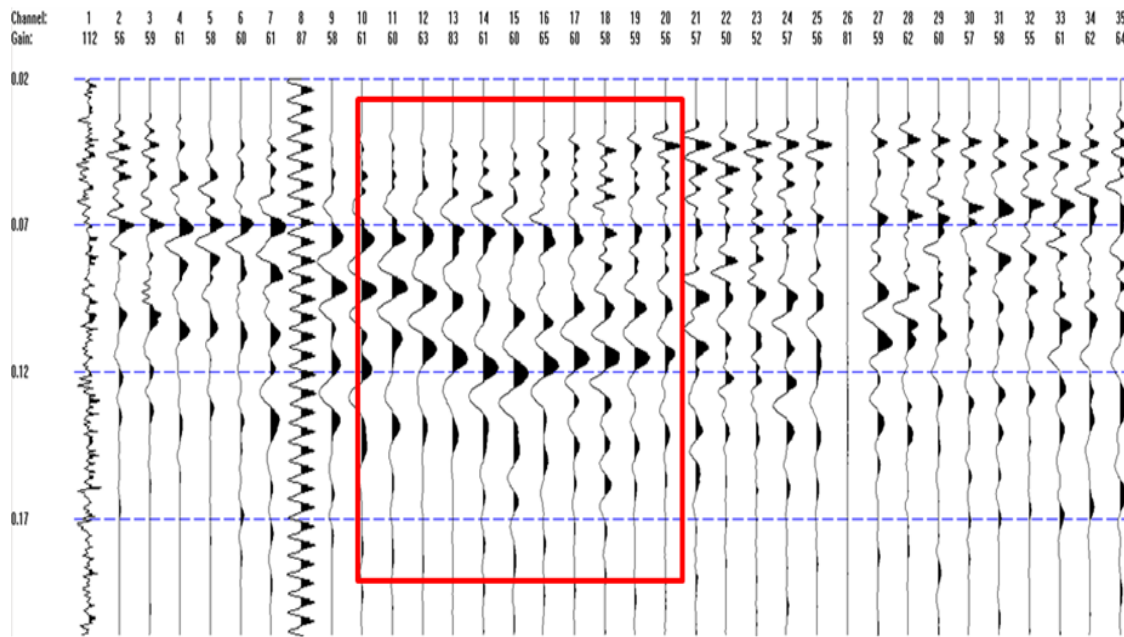


Figure 10. Seismogram record from the second fan-geometry seismic experiment at the Mason WMA field site. Thirty-six channels spaced at 3 meters were recorded at 500 μ s for a total record length of 512ms. Channel 1 is the source trigger. Channel 8 is defective. Late-arriving, large amplitude signals identified as trapped waves within the fault zone and highlighted in red.

Shot records from the lengthened seismic line, as highlighted by the red rectangle in Figure 10, indeed reveal a zone of disturbance between geophones 11 and 20. This zone of disturbance is characterized by late-arriving, large-amplitude, low-frequency wavetrains. Based upon characteristics of fault trapped waves, as presented in the literature, the distorted signals are tentatively interpreted as such.

A second set of seismic lines was collected on December 15, 2011. They were placed in approximately the same locations as the previous seismic experiments. An end-fire fault-parallel geometry was used in the acquisition of these lines instead of the fault-crossing fan geometry. These straight lines of evenly spaced geophones were located in three areas, as illustrated in Figure 11. One line was collected entirely in the Hickory Sandstone, one line entirely in the putative fault zone, and the third was located entirely within the crystalline basement rock. These straight-line geometries are intended to characterize the wave development and frequency content within the two separate lithologies, as well as aid in identifying a guided wave in the fault zone area.

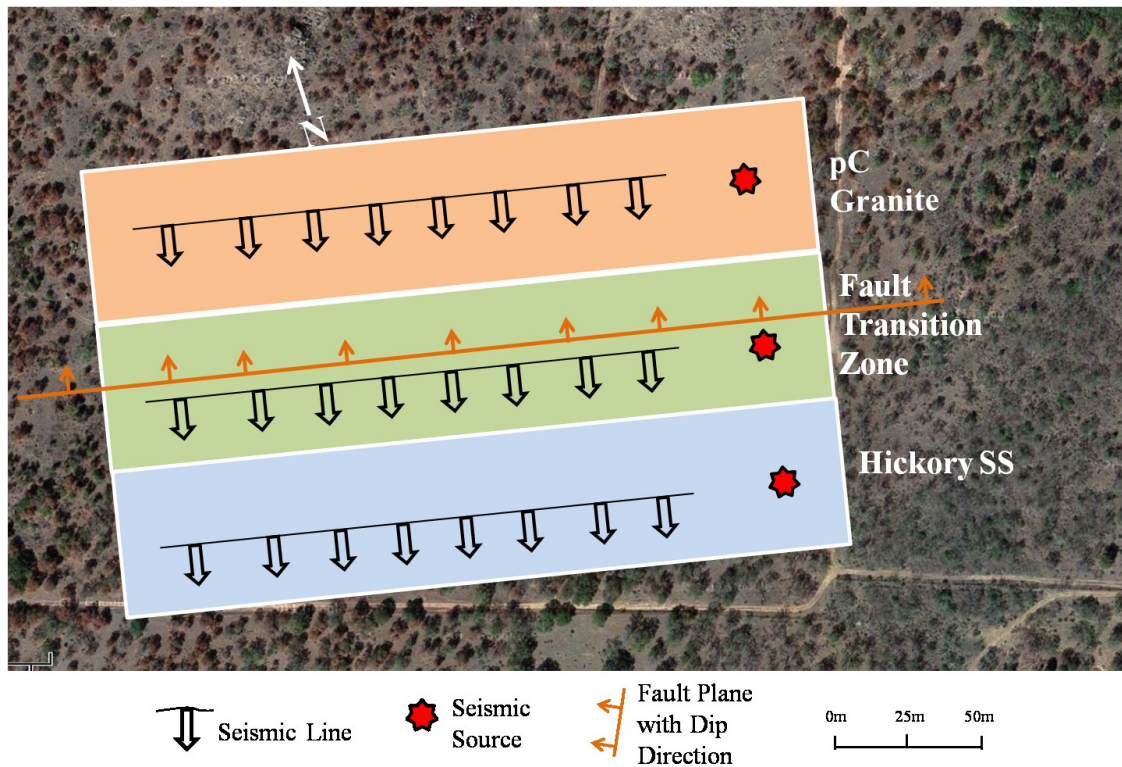


Figure 11. Diagram of second seismic experiment with end-fire acquisition layout. Acquisition geometries are overlain satellite photo, Figure 7, of field site. Three seismic lines were collected, one in each lithology and aligned parallel to the fault strike.

Each of the three seismic lines was collected multiple times with increasing sample rates and record lengths. The 512 ms records, recorded at a rate of 500 μ s, prove to be the most useful for interpretation. The same processing techniques were applied to each data set, including channel overlaying, t^2 gain application, low and high-pass filtering and spectral analysis. All seismic records contain a trigger signal (channel 1) that should be ignored as well as a defective channel 8.

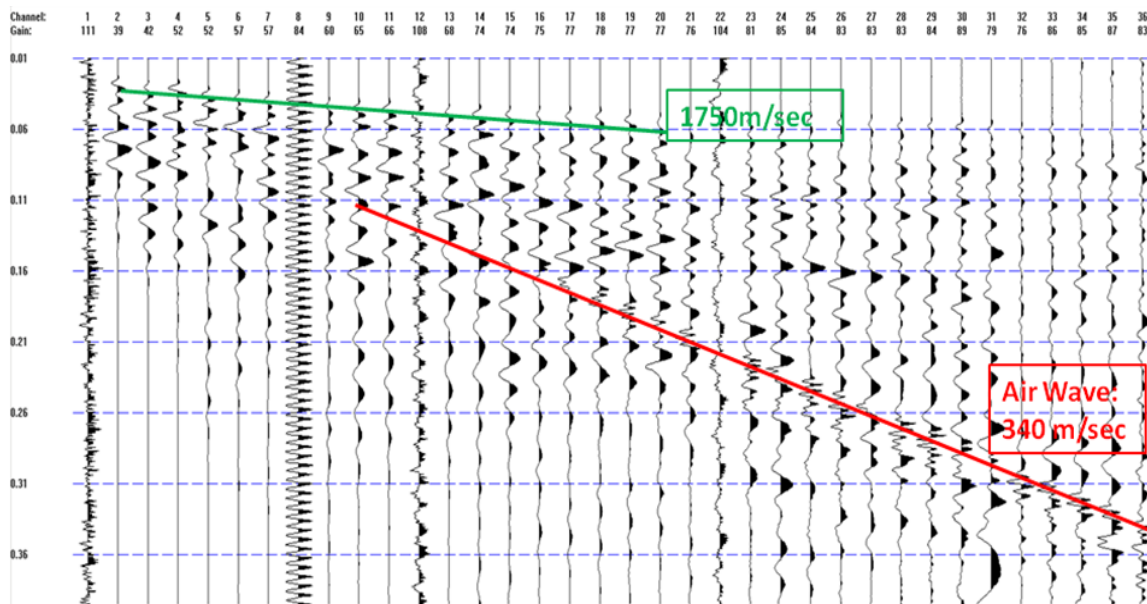


Figure 12. Seismic line collected in the Hickory Sandstone with 36 channels spaced 3.0 m apart. The red line shows the incoming air wave at a velocity of 340 m/s.

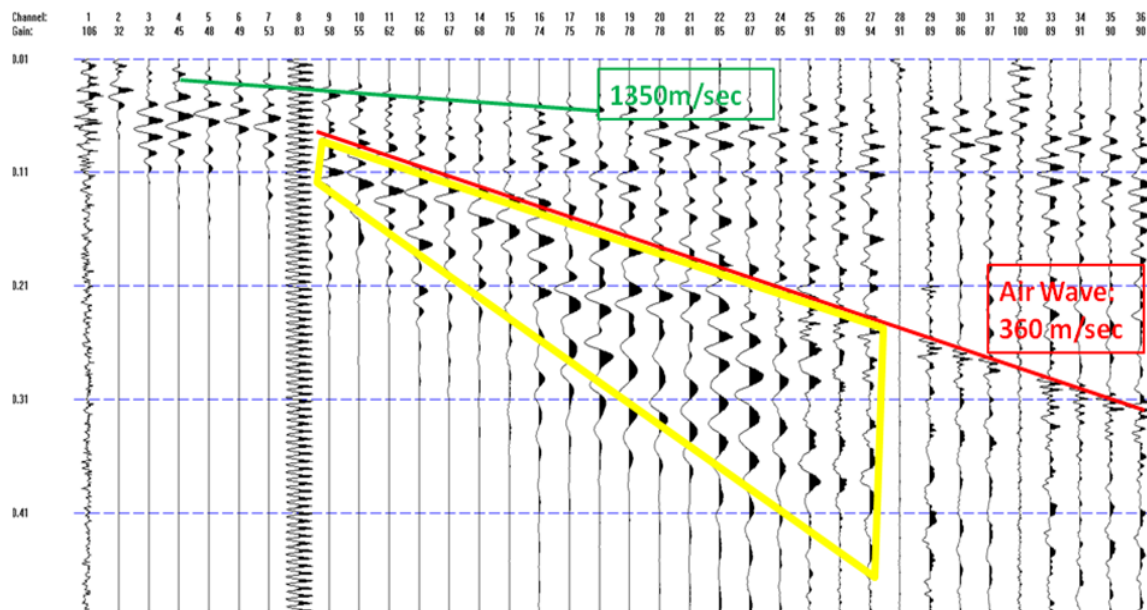


Figure 13. Seismogram collected along line within the proposed fault-zone. Air wave arriving at 360 m/s is highlighted in red. Dispersive wave packet of fault-trapped waves is boxed in yellow.

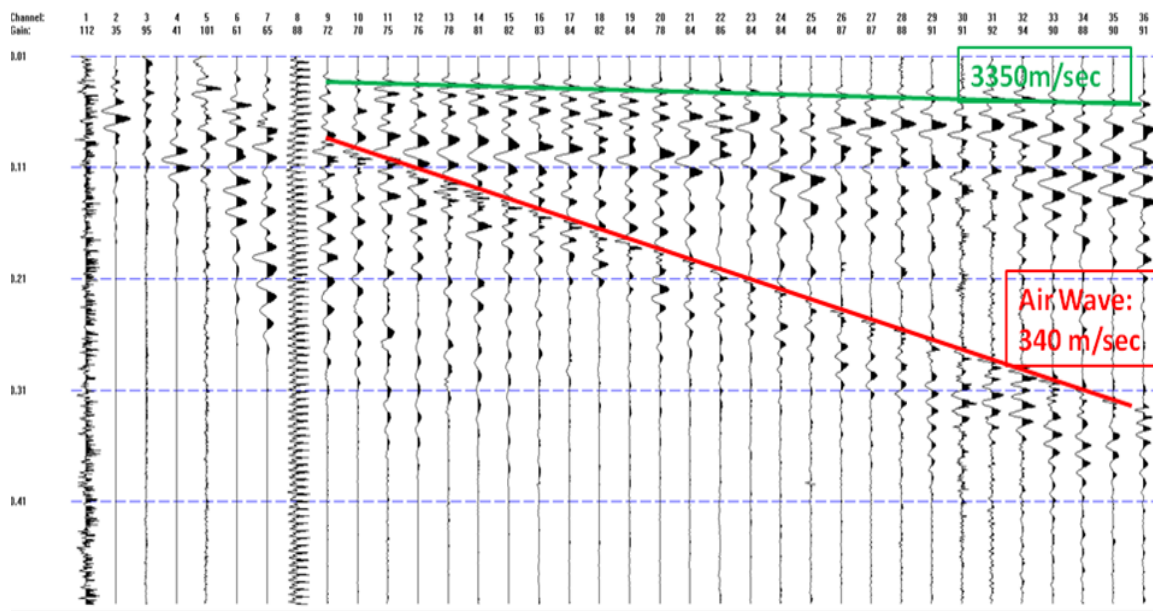


Figure 14. Seismic record for line located within granite at fault zone site. Air wave is highlighted in red.

The raw unfiltered seismogram records from the three lithologies (Figures 12-14) show distinct waveforms. The records from the sandstone and granite lines (Figs. 12 and 14 resp.) exhibit coherent reflections characterized by linear moveout arriving before and after the air wave in the middle of the record. Although the seismogram shown in Figure 12 retains some signal after the air wave breaks, they are not stronger than the earlier-arriving amplitudes. This can be explained by geometric spreading of the wave energy within a relatively homogeneous lithological unit. The consolidated material (sandstone and granite) comprising the footwall and hanging walls provides an efficient pathway for energy propagation with no internal reflections or scattering. This effect is

particularly evident in Figure 14 as signal amplitudes in the granite rapidly diminish after 0.15 s.

A region of increased amplitudes is easily seen in the fault-zone seismogram Figure 13, highlighted in yellow. Relatively coherent reflections are apparent within the highlighted zone through 150 ms. The dispersive signal, highlighted in yellow, may be due to a transition from the weathered surface layer into more consolidated fault structure at depth. The distinct dispersive wave packet, appearing after the air wave, is outlined by the yellow box in Figure 13 is interpreted as a dispersive packet of fault-trapped waves.

Figures 12-14 also display the computed seismic velocities for the three investigated lithologies. The relative change between the footwall sandstone and granite unit is a 47% reduction. The velocity contrast between the fault zone and the sandstone is 22% while the contrast with the granite unit is 60%. These values certainly present a sufficient velocity contrast between the rock units to produce guided waves. Li and Vidale found that a 40% velocity contrast should produce stronger guided-wave arrivals than a 15% reduction (Li and Vidale, 1996).

Overlay plotting of selected record channels was used to explore differences in amplitude between the seismic records collected in the three lithologies. A time-squared gain function $f(t^2)$ was applied to better resolve later arriving signals. The application of this function has been shown in the literature to improve identification of trapped-waves in seismic records (Shtivelman et al., 2005).

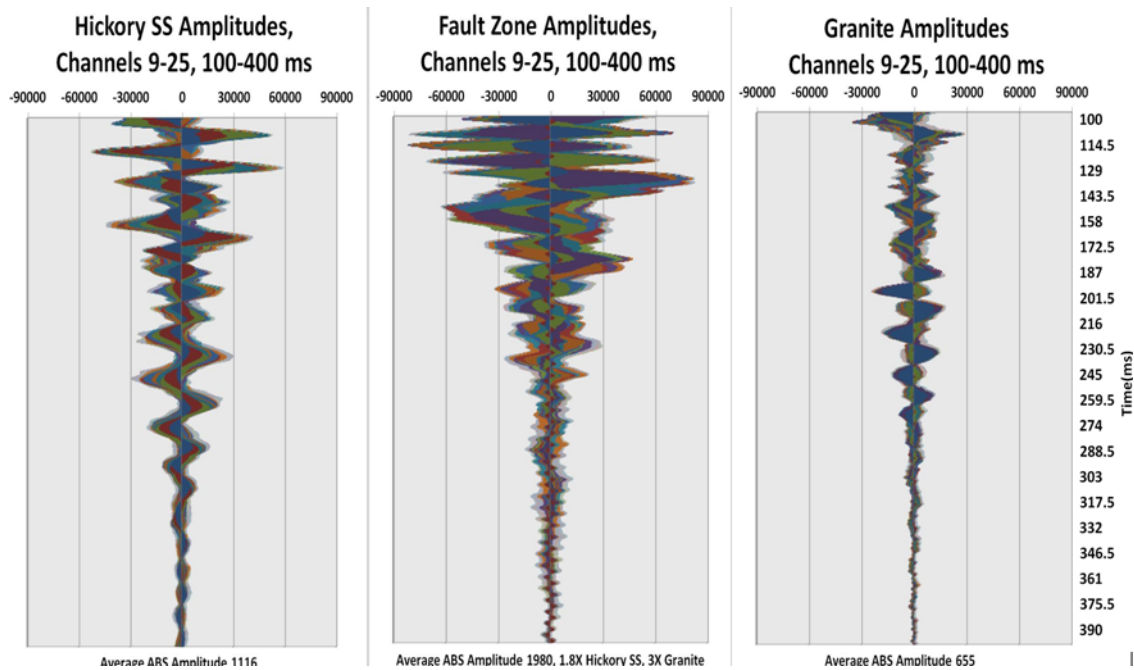


Figure 15. Overlay plots of seismic traces for the three lithologies tested. The true amplitudes of the traces were used. All plots are scaled the same.

Figure 15 displays three plots, one each for the hanging and footwall of the fault and another, in the middle, for the fault zone. The plots show the true amplitude values of channels 9-25 in the time interval 100-390 ms. The plot on the left, seismic traces from the Hickory Sandstone, displays early-arriving high-frequency traces with strong amplitudes that diminish rapidly into lower-frequency traces near the end of the record. The plot representing seismic traces from the granite, on the right side, displays a similar character but with weaker amplitudes. The center plot, from the fault zone, shows seismic traces with much larger, dispersive amplitudes throughout the first half of the time interval. The second half of the record is dominated by significantly weaker amplitudes of higher frequency content. The numerical values of the amplitudes can also

be compared between the three plots. The fault zone produces amplitudes nearly twice the values in the Hickory Sandstone unit and three times the strength of the granite signals. The fault zone produces higher amplitude signals throughout most, or the entire time interval. These signals are interpreted to be caused by fault-trapped waves.

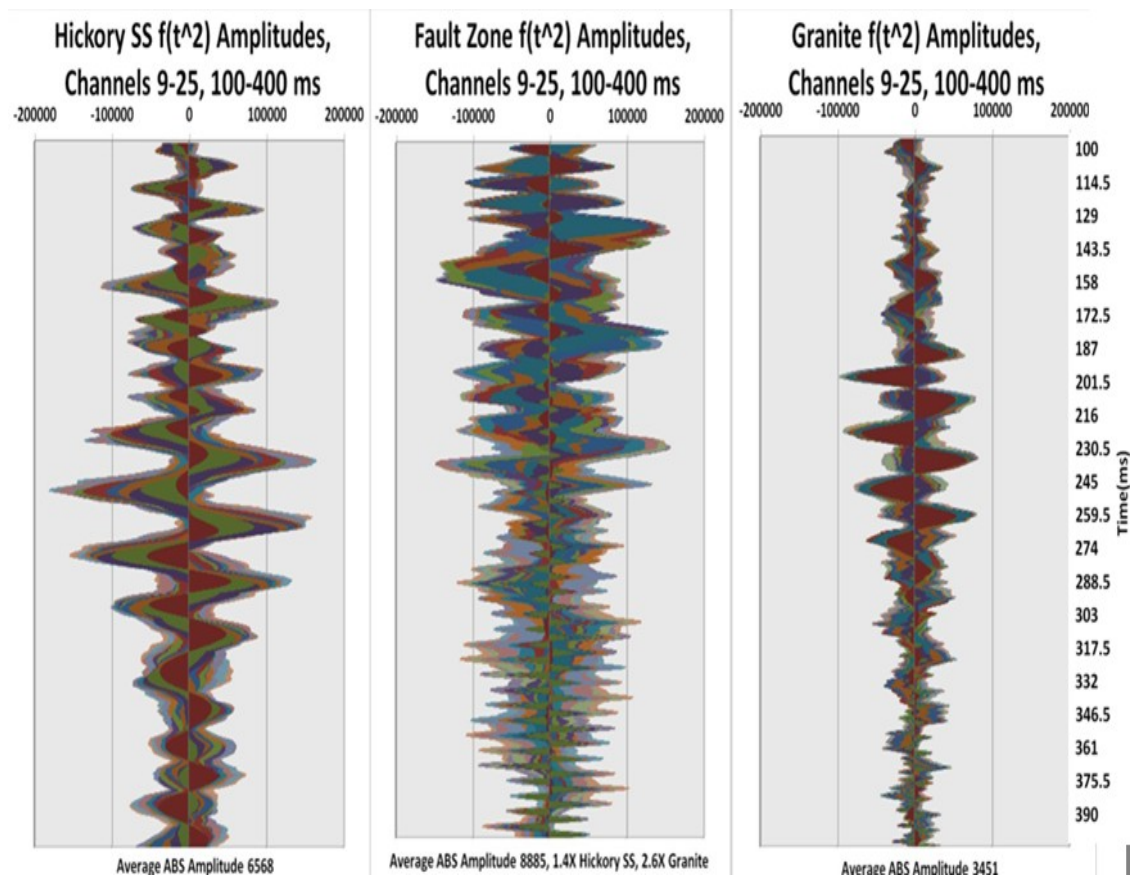


Figure 16. Overlay plots of $f(t^2)$ seismic traces for the three lithologies tested. True amplitudes of traces were enhanced. All plots are scaled the same.

Figure 16 shows graphs of the same data presented in Figure 15, except the seismic amplitudes have been multiplied by the squared-time gain factor. The application of the t^2 function enhances late-arriving signals and assists in the interpretation/identification of fault-trapped waves (Shtivelman et al., 2005; and Li and Vidale, 1996). When comparing the three plots of Figure 16 it is clear that the fault zone again produces the highest amplitude signals. The middle plot displaying the seismic traces from the fault zone maintains strong amplitudes throughout the entire time interval and shows what may be interpreted as a dispersive, low to high frequency, wave packet. The Hickory Sandstone and granite plots show increased amplitude responses in the middle of the records, purely in response to the applied t^2 function. Also, amplitudes within the fault area are at least an order of magnitude larger than the sandstone and granite signals. Signals within the fault zone develop into a high-amplitude dispersion pattern throughout the entire time interval.

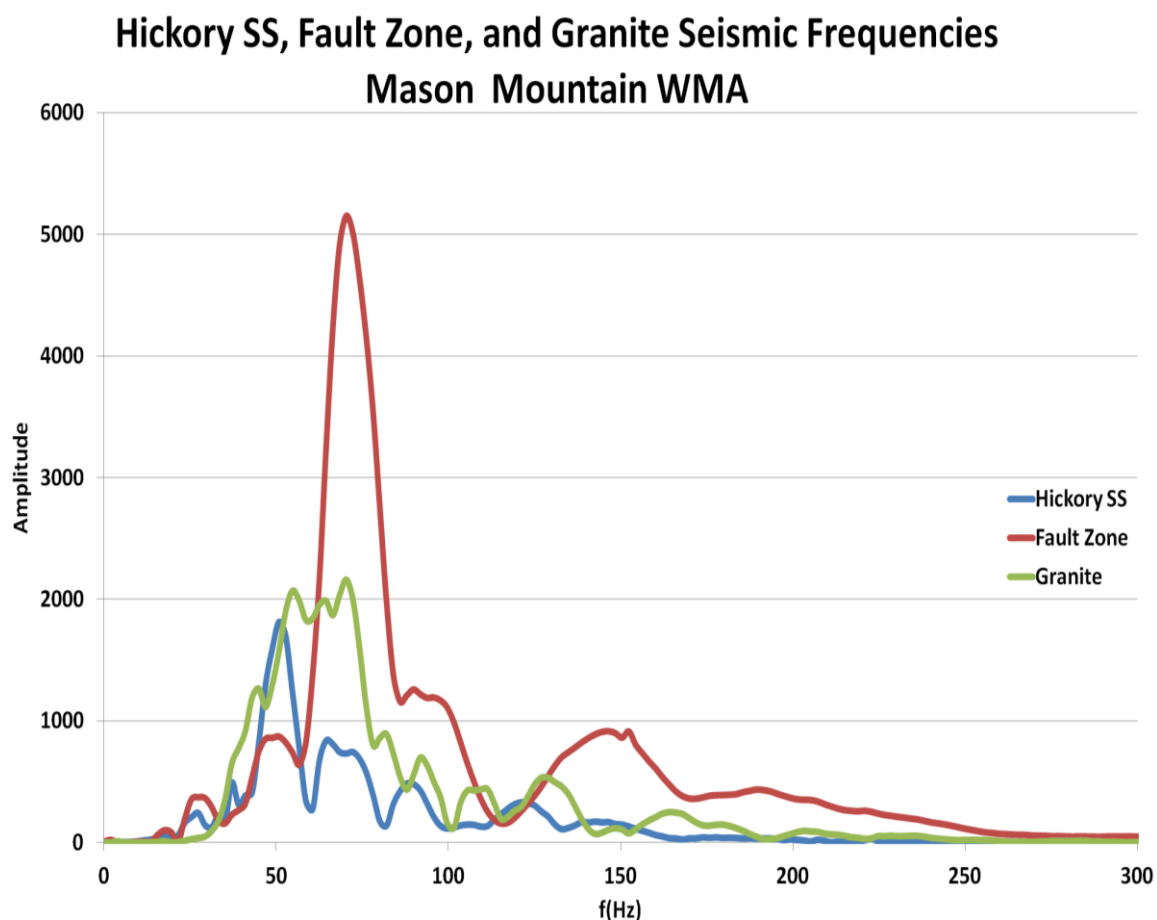


Figure 17. Frequency spectrum of the three lithologies, Hickory Sandstone, fault zone, and granite. True amplitudes were used in the Fast Fourier Transform (FFT) to extract the $f(\text{Hz})$ vs. amplitude content.

Figure 17 shows amplitude spectra for all three seismic lines. A fast Fourier transform (FFT) was applied to all three data sets using the original amplitude values. As shown earlier, the fault zone data presents stronger amplitudes compared to the sandstone and granite data. The fault zone data show two frequency peaks, a primary one at 70 Hz and a higher frequency secondary peak at 145 Hz. Secondary peaks are not clearly evident on the other two spectra.

Based upon the computed seismic velocities shown in Figures 12-14 and the amplitude spectra shown in Figure 17, the seismic wavelength λ and fault-zone width w can be estimated. When the computed seismic velocity for the fault zone, 1350 m/sec, is used in conjunction with the center frequency for the fault zone, 70 Hz, the seismic wavelength is found to be 19.3 m. A widely accepted rule of thumb is that a seismic wavelength of roughly the same width of a waveguide ($\lambda/w=1$) is required to produce guided waves. Recent publications exploring features of fault guided waves through numerical modeling have also found that this 1:1 ratio produces strong and clearly identifiable fault guided waves. A 3:1 ratio of wavelength to fault width has been found to work as well (Li and Vidale, 1996). The dominant seismic wavelength of the second seismic experiment leads to a favorable λ/w ratio since the surface geological evidence indicates that the fault zone is ~20 m wide.

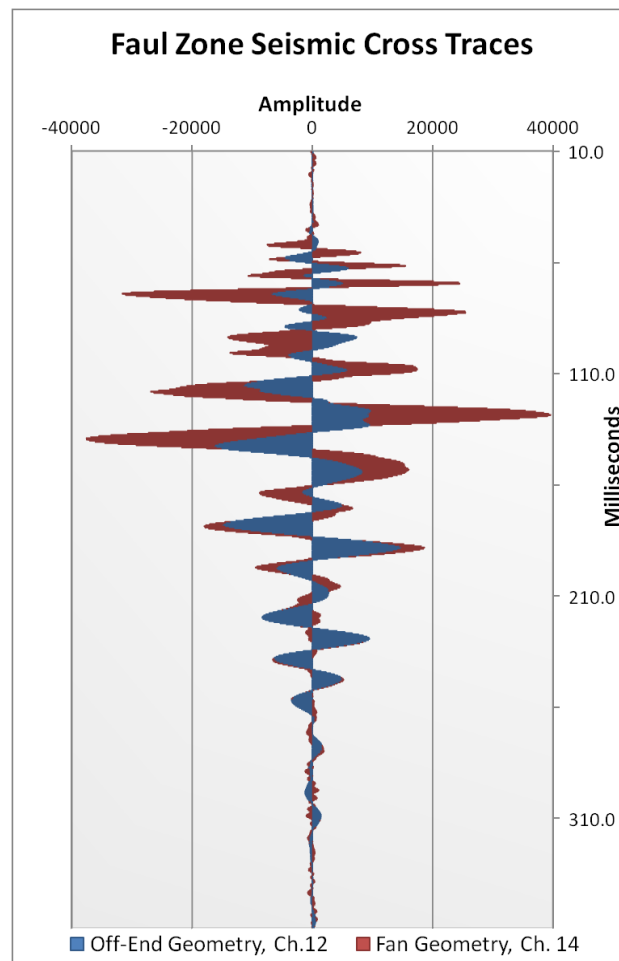


Figure 18. Traces from fan geometry and off-end geometry seismic lines, located in fault zone, which cross to tie the collection lines together. The trace signals conform to one another well and show a common signal between the two collection lines. Traces between 50 and 100 ms and 110 and 200 ms match well.

Figure 18 shows two traces, channel 12 from the fault zone end-fire seismic line and channel 14 from the fan geometry seismic data, equally gained and with the same time windows. These two traces from different seismic lines are characterized by

identical shotpoint and geophone locations. The two trace amplitude variations are well-correlated, as expected.

Additional seismic records were collected during February 2012 as the seismoelectric experiment was being completed. There were several differences between these seismic experiments and the previous tests. The geophones used in acquiring the February seismic data had a center frequency of 28 Hz. The seismograph was a Geometrics Geode. Although the geophone spacing was increased to 4.0 m, the source remained the same, a 3.6 kg sledgehammer. A large difference also occurred in the soil conditions as the February data were collected after the area experienced large amounts of rainfall resulting in ground saturation. The seismic shot records were stacked 40 times. Straight seismic lines in only the fault zone and the granite were collected as there was insufficient time to acquire data in the sandstone. Noise from the seismograph trigger and geophone channel cross-talk infiltrated the seismograms and lowered the quality of the data. Figure 19 shows a stacked seismic record collected in the fault zone. The air wave is highlighted as well as the first break picks. The latter reveal a nominal material velocity of 1390 m/s, conformable to the velocity found in the earlier seismic experiment (Figure 13). A dispersive wave packet of high amplitudes, similar to those seen in Figure 13, is fairly clear. This packet is interpreted as the signature of critically reflected guided waves trapped within the fault zone.

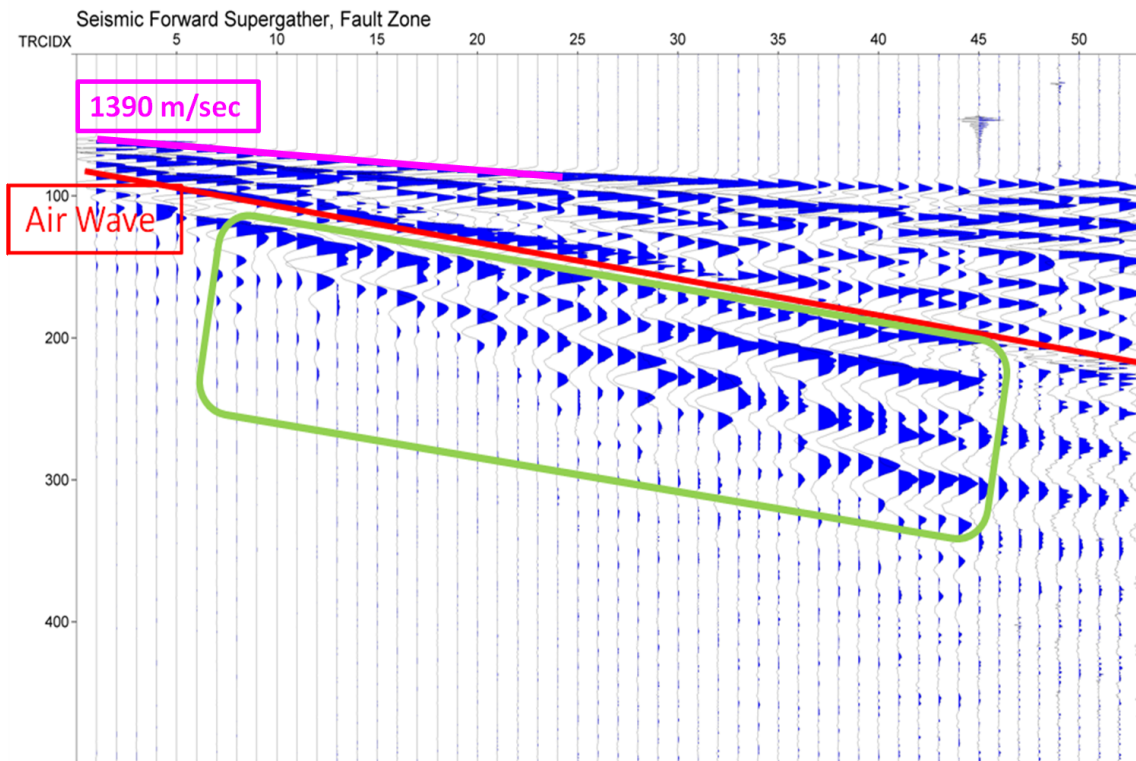


Figure 19. Seismogram of February seismic data collected in fault zone. Material velocity of 1390 m/s highlighted in pink. Late incoming packet of traces with some dispersion pattern is evident after the air wave, circled in green box.

In contrast, shown in Figure 20 is a record of seismic data from the granite area. Once again, the material velocity computed from the first-break picks matches the velocity of the granite found in the previous seismic experiment (Figure 14). Compared to the record shown in Figure 19, there is a clear difference in the amount of energy arriving after the air wave. The granite record loses amplitude content with offset while the fault zone record shows increased amplitudes with offset and time-depth.

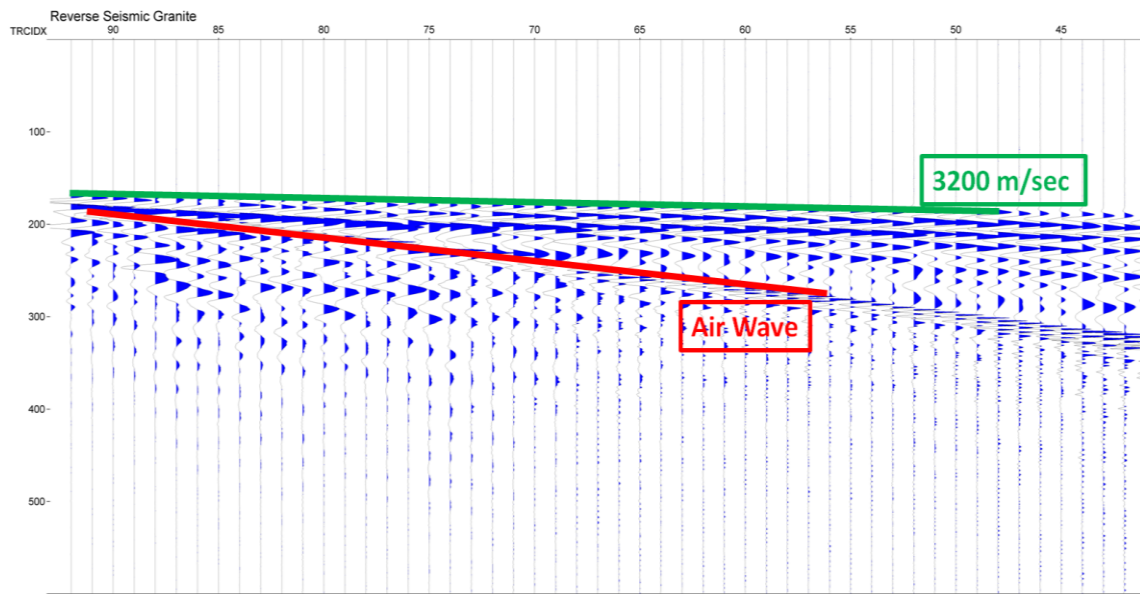


Figure 20. Seismic record shot within the granite basement lithology. The incoming air wave is clearly seen, highlighted in red. Material velocity highlighted in green. Low amounts of energy are evident after the air wave.

SEISMOELECTRIC DATA ANALYSIS

The primary seismoelectric data for this research were collected in February 2012. Dr. Karl Butler of the University of New Brunswick (UNB) provided specialized equipment for the data collection, as well as extensive knowledge of the acquisition procedure and processing/analyzing techniques. The same field site at the Mason Mountain Wildlife Management Area was tested.

Equipment provided by UNB included three 12-channel Geometric Geode seismographs, 25 custom built preamplifiers, and associated cables, data acquisition, and processing software. Stainless steel rods were used as electric dipole sensors. The seismic sources used included the same 3.6 kg sledgehammer from the previous seismic experiments as well as a 40 kg accelerated weight drop. The large weight drop, powered by a 12-volt marine battery and driven by elasto-polymer bands was tested at the field site but did not produce useful results. The heavy rainfall immediately prior to data collection caused the strike plate to sink into the ground. Positioning the trailer-hitch-mounted weight drop proved difficult in the muddy conditions. Figure 21 shows a picture of the weight drop being tested at the field site. Test data showed that the weight drop introduced negligible amounts of additional seismic energy when compared to the sledgehammer source. The elastically propelled system also created a secondary source impact due to the rebound of the elastic firing bands.



Figure 21. Weight drop mechanism mounted to back of vehicle at field site. Source was a PEG AWD of 40 kg weight.

Past seismoelectric experiments simultaneously collected data with alternating geophones and electrode dipoles on a single seismic cable so that both seismoelectric and seismic data sets are acquired under the same conditions. Due to time constraints and the possibility of contamination of the seismoelectric data by movement of the geophone magnets, we acquired seismic data and seismoelectric data separately. Due to

rainy weather conditions and equipment availability, the seismoelectric data were collected only within the fault zone and associated granite, but not in the sandstone.

The electric preamplifiers utilized in the seismoelectric data collection were designed, built, and tested by Dr. Butler during his PhD research at the University of British Columbia. He has since utilized them in recent seismoelectric investigations at UNB. The purpose of the preamplifiers is to decrease the noise to signal ratio and to heighten the sensitivity of the recorded data, thereby amplifying the minute seismoelectric signals. The preamplifiers were built with high input impedance ($2\text{ M}\Omega$ differentials), a gain multiple of 30X, and a 2 Hz — 30 kHz bandwidth (Butler, et al., 1996).

Each seismoelectric line consisted of 23 contiguous dipoles of length 4.0 m. This dipole length was chosen on the basis of the fault zone geometry and available cable lengths. As previously described, surface geological investigations as well as interpretation of the seismic data provided estimates of the fault zone width as $\sim 20\text{ m}$. The length of the electrode dipole has been shown to impact the magnitude of recorded amplitudes for certain wavelengths in seismoelectric experiments (Haines, 2004). Haines' schematic, shown here as Figure 22, displays this concept. An electrode dipole length equal to the wavelength of the signal of interest will record a zero amplitude signal. An electrode dipole length one half of this wavelength records a maximum signal. This concept is applied to relate dipole length to signal frequency. Since two types of seismoelectric signals, the direct field and interface response, arrive at electromagnetic velocities, the dipole length spans many wavelengths of these signals.

The coseismic field traveling at seismic velocities however must be considered when planning the dipole length. It was determined that the dipole spacing would not affect the measurements due to the very large difference in dipole length and seismic wavelength at the Mason WMA site. The dipole length is 4.0 m while the expected dominant seismic wavelength is ~ 25 m.

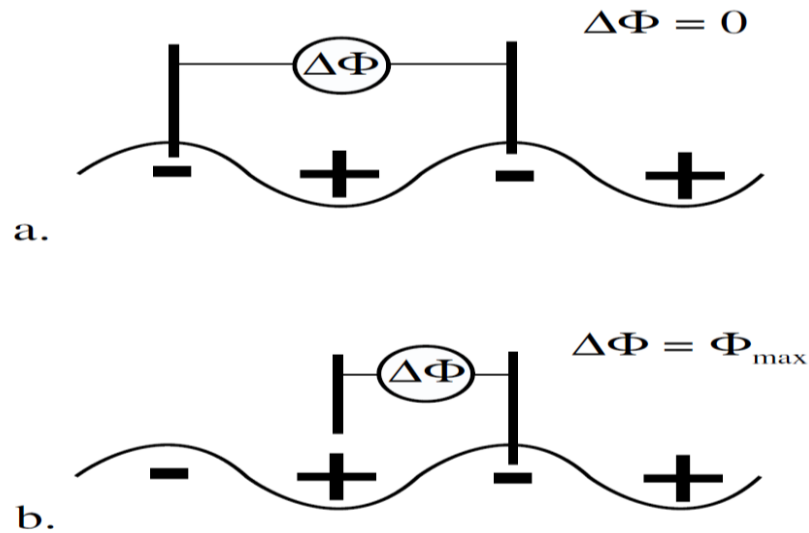


Figure 22. Relationships between electrode spacing and coseismic wavelengths recorded. (a) Dipole width equals seismic wavelength resulting in no measured signal. (b) Dipole width is one-half the wavelength, maximum signal is recorded. (Haines, 2004)

Care must be taken in seismoelectric experiments to avoid creating stray electromagnetic fields. For example, the generation of a Lorentz field, shown in Figure 23, was avoided by using a plastic strike-plate generation in place of a metal plate. A

metal strike-plate would have generated a local electric field as the conductive mass moves through the Earth's magnetic field. Although electrical insulation between a metal plate and the ground has been shown to eliminate the Lorentz field, we avoided this issue by employing a plastic strike-plate.

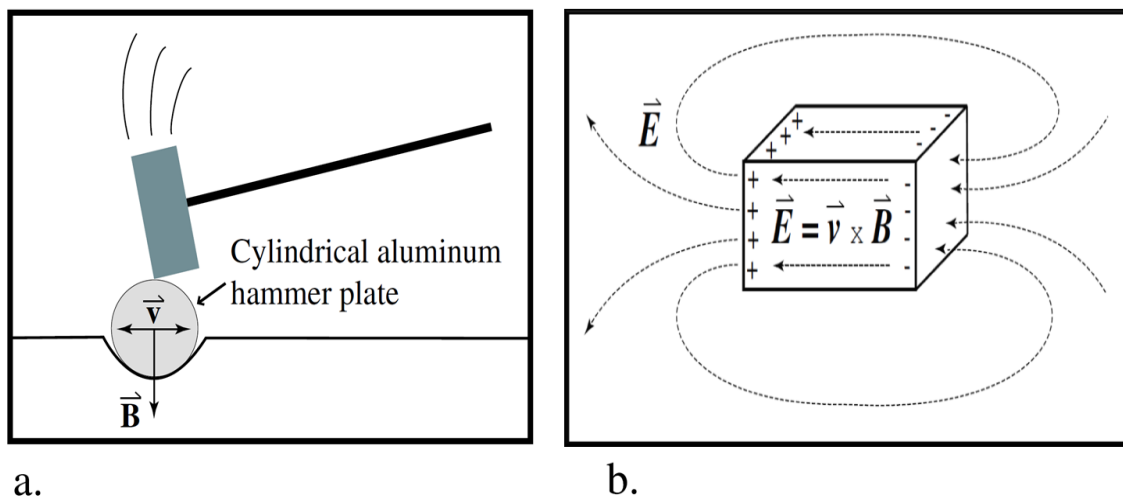


Figure 23. Side (a) and perspective (b) views of the Lorentz field created by striking a metal plate and hammer for a seismic source. Image on the left illustrates the hammer striking a cylindrical aluminum plate. The plate may be any shape or composed of any conductive material. Image to the right shows the proposed metal plate, of any shape, creating an electric field, E , as the conductive material moves, with a velocity v through the Earth's magnetic field, B . (Haines, 2004)

The seismoelectric data collected in February 2012 were acquired using the same straight-line geometry as the November 2011 seismic experiments. No fan seismoelectric layouts were attempted. The two straight lines of 23 dipoles of length 4.0

m were co-located with the fault-zone and granite seismic “end-fire configuration” lines.

Figure 24 depicts the acquisition geometries for the seismoelectric data.

Two remote orthogonal dipoles located ~300 m west were also deployed simultaneously to record regional noise. These dipoles were also 4.0 m in length. The remote dipole data were later used to subtract regional noise and sferics.

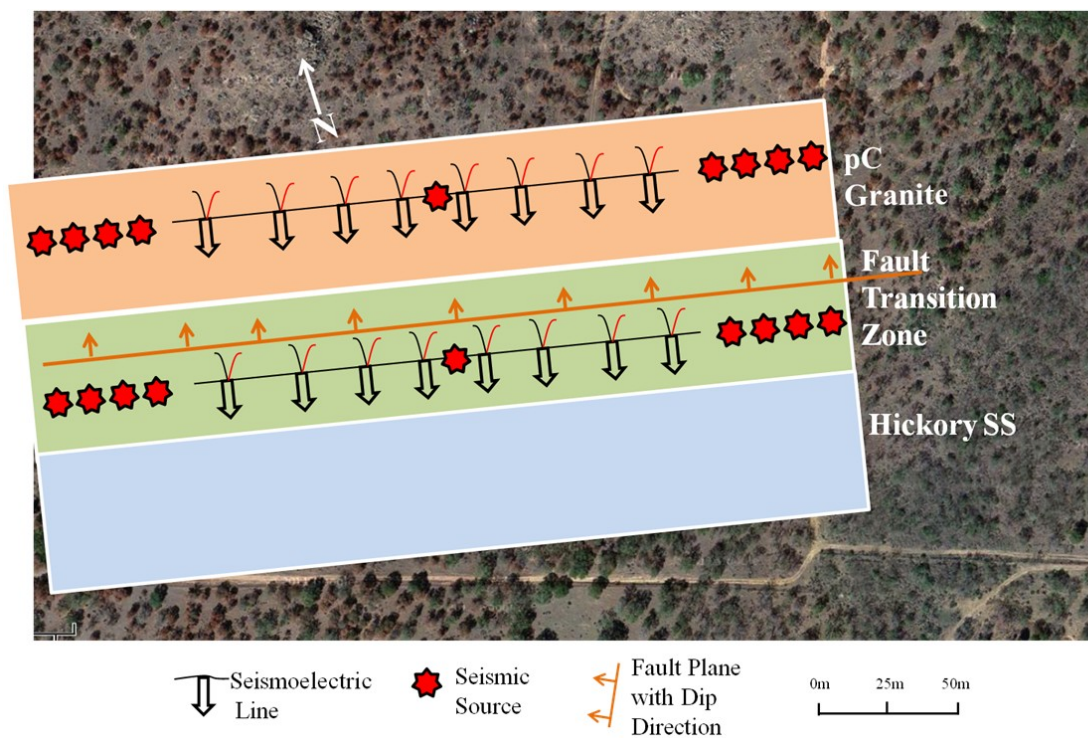


Figure 24. Map view illustration of the two seismoelectric collection lines overlain atop lithology zones and satellite photo of field site.

As shown in Figure 24, the two lines of seismoelectric data each utilized 9 shotpoint locations. Four shot locations were located 4.5, 5.5, 6.5, and 7.5 m off each

end of the receiver lines, as well as one shot located in the middle of the spread. Each shot was stacked 40 times using a sledgehammer. The four groups of off-end shots enabled supergathers to be assembled prior to the processing of the data. These supergathers are possible by maintaining a common spacing between the four shots and locating the four shots within a dipole-length, 4.0 m. Therefore, each of the shot points provides a unique source-receiver offset. The middle shot was collected to investigate lateral heterogeneities within each of the two different lithologies.

The primary data processing techniques applied to the seismoelectric data were performed by Dr. Butler of UNB, as he is familiar with the processes, has developed a processing workflow, and is familiar with common processing problems and resolutions. Dr. Butler applied harmonic subtractions for up to 9 modes (nine multiples of the primary 60 Hz harmonic noise), a tapered surgical mute to cut out trigger crosstalk at time zero when necessary, and causal Butterworth bandpass filters (14 Hz/12 dB/octave – 200 Hz/24 dB/octave). Regional spherics and noise were identified from the remote dipoles and deleted from all data.

As previously mentioned, surface waves are not a focal point of this research, and their effects were assumed to be negligible. The absence of strong ground roll motion from the nearest offset traces argues against a surface wave interpretation of the seismoelectric signals. Shear waves are also not considered in the data collection or interpretation. The electric field generated through induction, by shear wave propagation, is thought to be insignificant compared to the streaming current produced

by compressional P waves (Pride and Haartsen, 1996). For these reasons, we assumed in this research that any seismoelectric conversions were caused by P waves.

To interpret the seismoelectric data collected at the WMA site, I first examined the supergathers constructed, with the invaluable assistance of Dr. Butler, for each set of forward and reverse facing shots. A supergather labeled “forward shot” refers to the line collected when the shot points were located on the road. “Reverse shot” gathers refer to data lines collected when the source shots were located in the woods to the west. I interpreted the reverse and forward supergathers of seismoelectric data from both the fault zone and granite area.

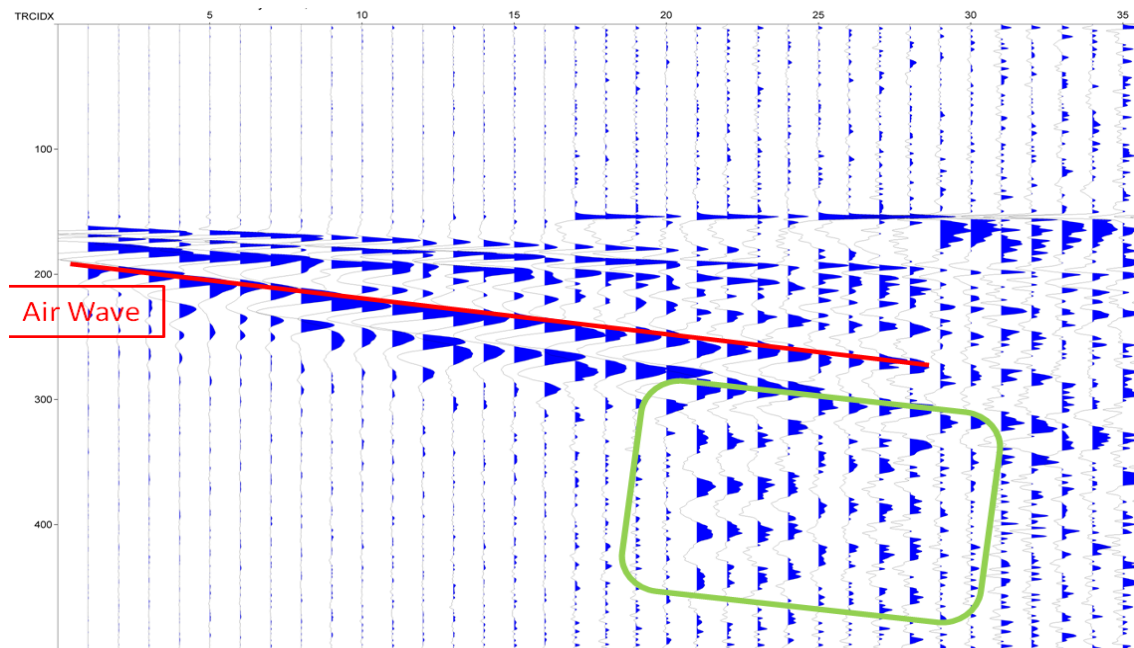


Figure 25. Forward shot seismoelectric supergather collected in fault zone. The propagating air wave is highlighted by a red line. Area of interest, anomalous late-arriving large-amplitude signals, circled in green.

Figure 25 shows a forward-shot seismoelectric supergather collected in the fault zone. No clean arrival of late-arriving dispersive energy is seen in this seismoelectric supergather, but a packet of anomalously-high amplitude energy is evident after the strong air wave, as highlighted by the green rectangle. This packet is consistent with the temporal and spatial location of the guided wave interpreted from the seismic records. Another explanation for the sudden appearance of late energy at far offsets is that of refraction of guided waves within the fault zone (Wu and Hole, 2011). Figure 26 shows a second seismoelectric supergather collected in the fault zone, when the shots were located in the woods to the west where the hammer plate was placed on wet, poorly consolidated soil. This record shows a larger group of late-arriving high-amplitude traces than does the record shown in Figure 25. A possible explanation is the location of the shots being changed from the compacted road to the saturated soil. The high-amplitude signals arrive after the air wave. A clear dispersion packet is not clearly seen at far offsets on the record. This may be due to the significant signal to noise ratio decrease experienced at the farther offsets.

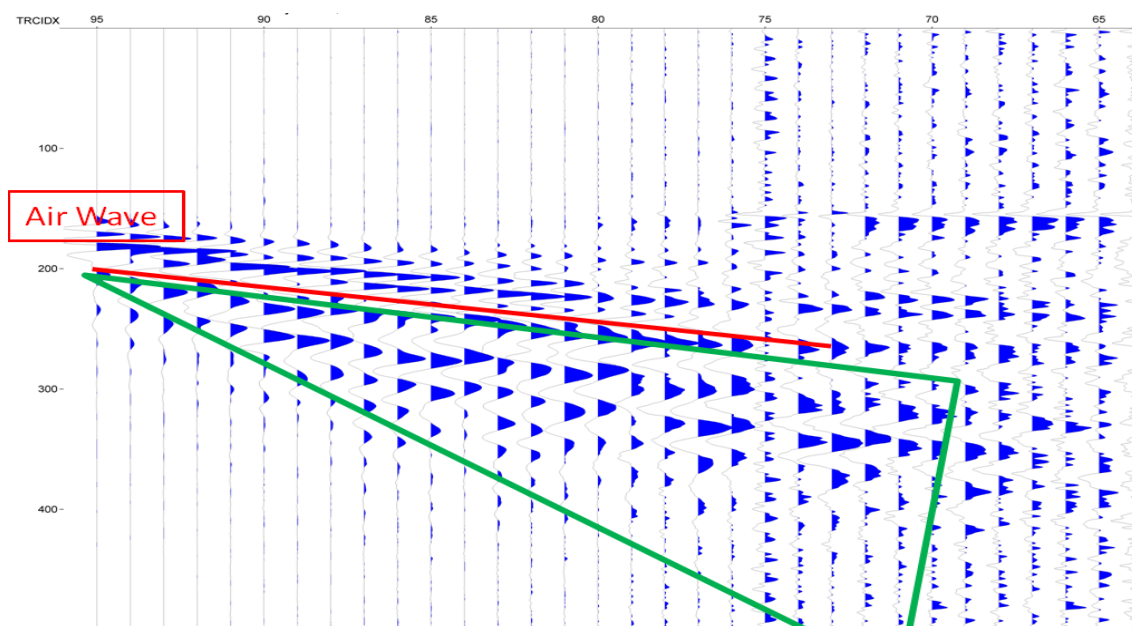


Figure 26. Reverse shot seismoelectric supergather collected in fault zone. Air wave is highlighted in red. Green triangle shows late-arriving energy consistent with a guided wave.

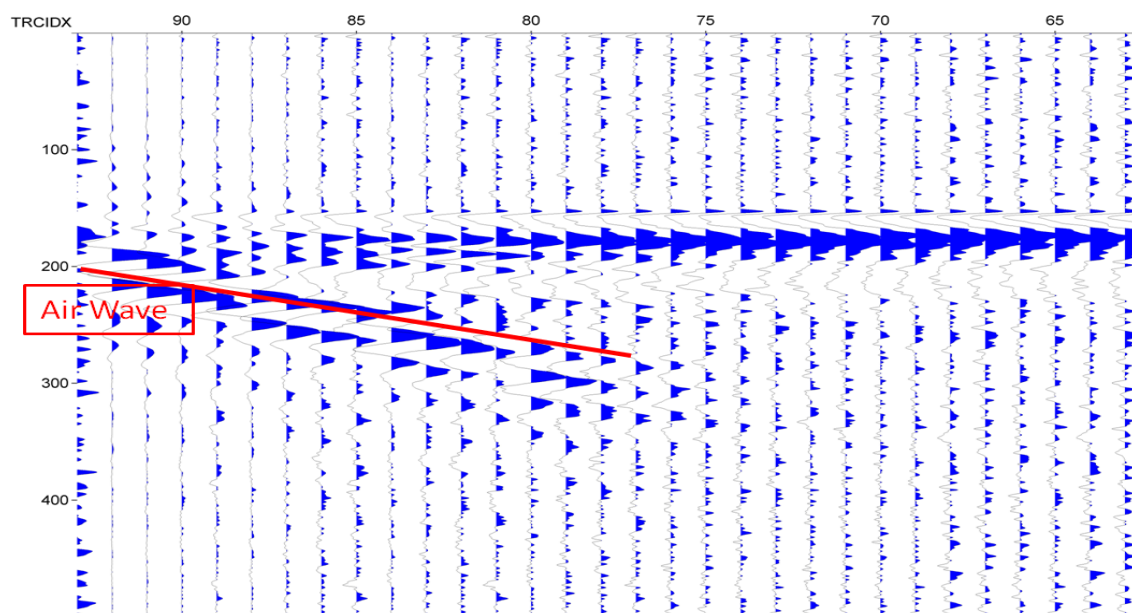


Figure 27. Reverse shot seismoelectric supergather collected in the granite. Air wave is highlighted in red.

Seismoelectric data collected in the granite show clear seismoelectric direct field energy (with almost zero moveout, as would be expected for signals traveling at electromagnetic velocity) and a strong incoming air wave. This record lacks a dispersive energy packet, as would be expected from fault-trapped waves. Figure 28 shows overlay plots of the trace amplitudes from the fault zone without gain applied, and then with a time-squared gain function applied. This process is used to enhance the late-arriving signals, such as guided waves. Figure 29 shows the same overlay plots of the granite data.

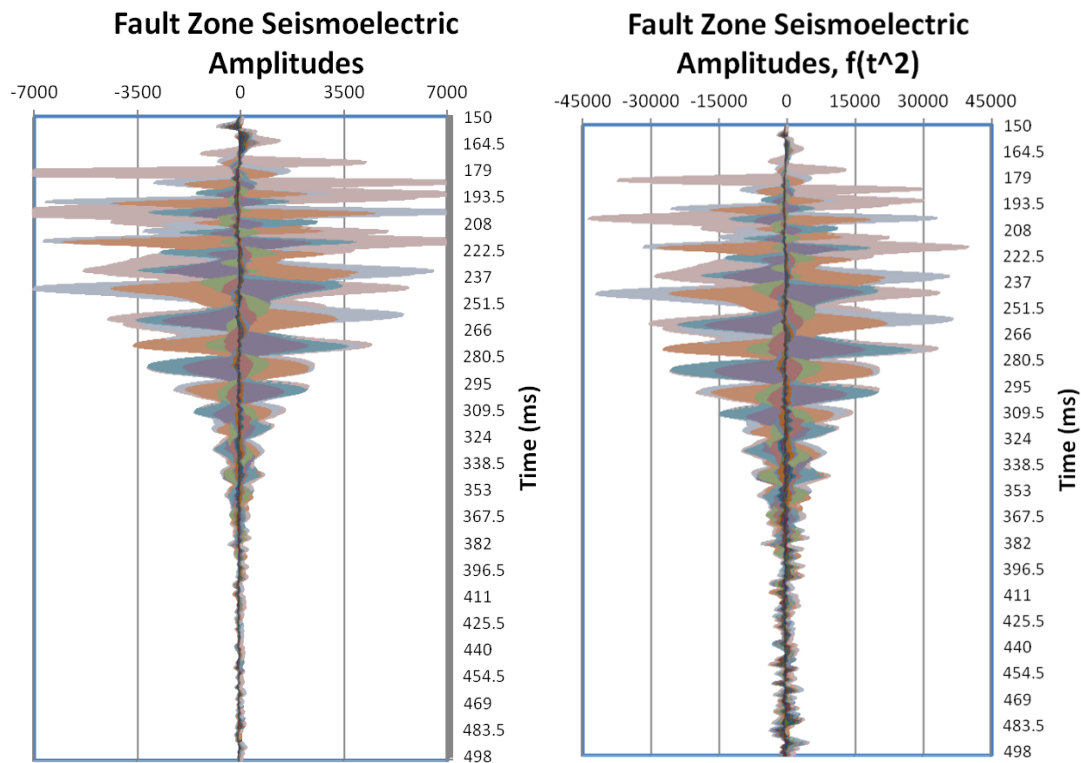


Figure 28. Overlay plots of fault zone trace amplitudes with and without time-squared function applied.

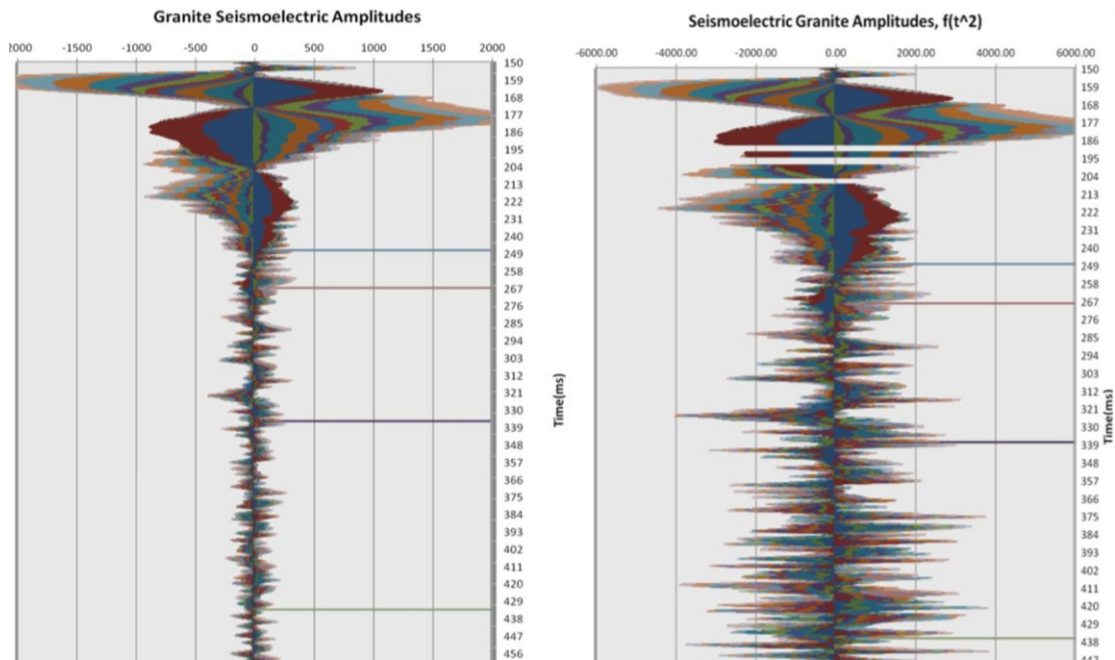


Figure 29. Overlay plots of granite seismoelectric trace amplitudes with and without time-squared function applied.

The overlay amplitude plots in Figure 28 and 29 reveal distinct differences between the fault zone and granite data. The fault zone produces traces ~ 3.5 times stronger compared to those of the granite record. Secondly, almost all of the large-amplitude signals in the granite plot are located between 150—250 ms, while the high-amplitude signals arrive later in the fault zone plot. These differences are also seen in the corresponding time-squared plots. Late-arriving data, after 300 ms, in the fault zone is enhanced by the gain function. When the gain function is applied to the granite data, only scattered high frequency noise is boosted. The t^2 plot shown in the right hand side of Figure 29 shows these high-frequency signals which have been increased in amplitude. They do not exhibit the characteristics of fault-guided waves.

DATA COMPARISON AND EVALUATION

Multiple seismic and seismoelectric data sets were collected and processed. They were interpreted independently based upon the capabilities of each dataset to generate guided waves. Viewing the data sets together and directly comparing them can distinguish whether the seismoelectric method produces and displays fault-guided waves.

Figure 30 shows a compilation of three stacked seismic records from the Hickory Sandstone, fault zone, and granite, respectively. These three records collectively demonstrate that conventional seismic techniques are very capable of imaging and distinguishing fault guided waves. A clear packet of dispersive guided wave energy, highlighted in yellow, is seen in the fault zone record, labeled A, while the other two records in the footwall and hanging wall display no similar traces. The previous Figures 15 and 16 display the amplitude responses of the seismic data. They also clearly show that the fault zone produces higher-amplitude signals than the corresponding sidewalls. After a time-squared gain function is applied, the interpreted guided waves in the fault-zone seismic record become more pronounced relative to the late energy in the sandstone and granite records. Figure 10 also displays the capability of the seismic method to resolve a fault zone using a fan-geometry in which geophones are located in all three lithologies.

Although the magnitudes of the amplitude anomalies representing the fault-guided waves cannot be compared between the seismic and seismoelectric data, because

the two data types record different physical mechanisms, the overlay plots presented in Figures 15,16, 28, and 29 demonstrate that the fault zone produces higher amplitude late-arrivals than the surrounding lithologies.

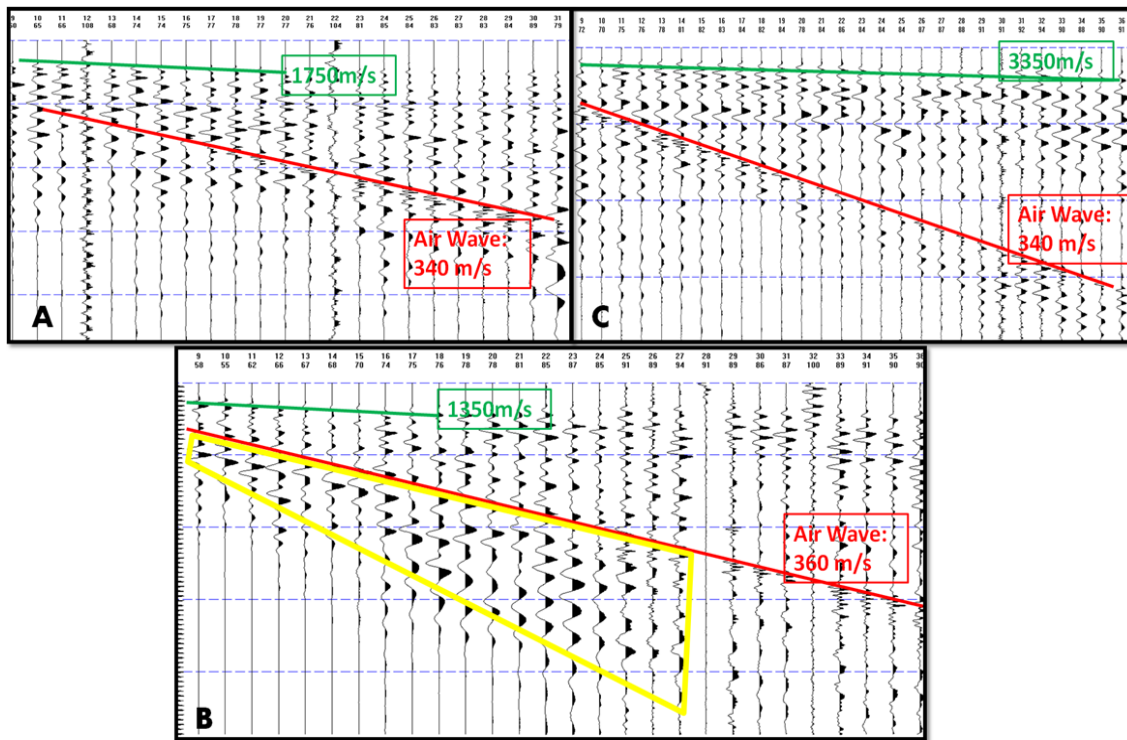


Figure 30. Three seismic records; (A) Hickory Sandstone, (B) fault zone seismic record, (C) granite seismic record. Green lines highlight first breaks and corresponding lithology velocities. Red lines highlight incoming air wave. Yellow box in plot B highlights interpreted fault-guided waves.

Figure 31 shows seismoelectric records collected atop the fault zone and in the granite zone. The seismoelectric results do not show the extreme and distinct differences in fault-guided energy as does the seismic data, Figure 30. The natural magnitude of the

seismoelectric signals present in the field due to the propagation mechanism may provide an explanation. However, the seismoelectric method is able to image some fault zone energy arriving after the air wave.

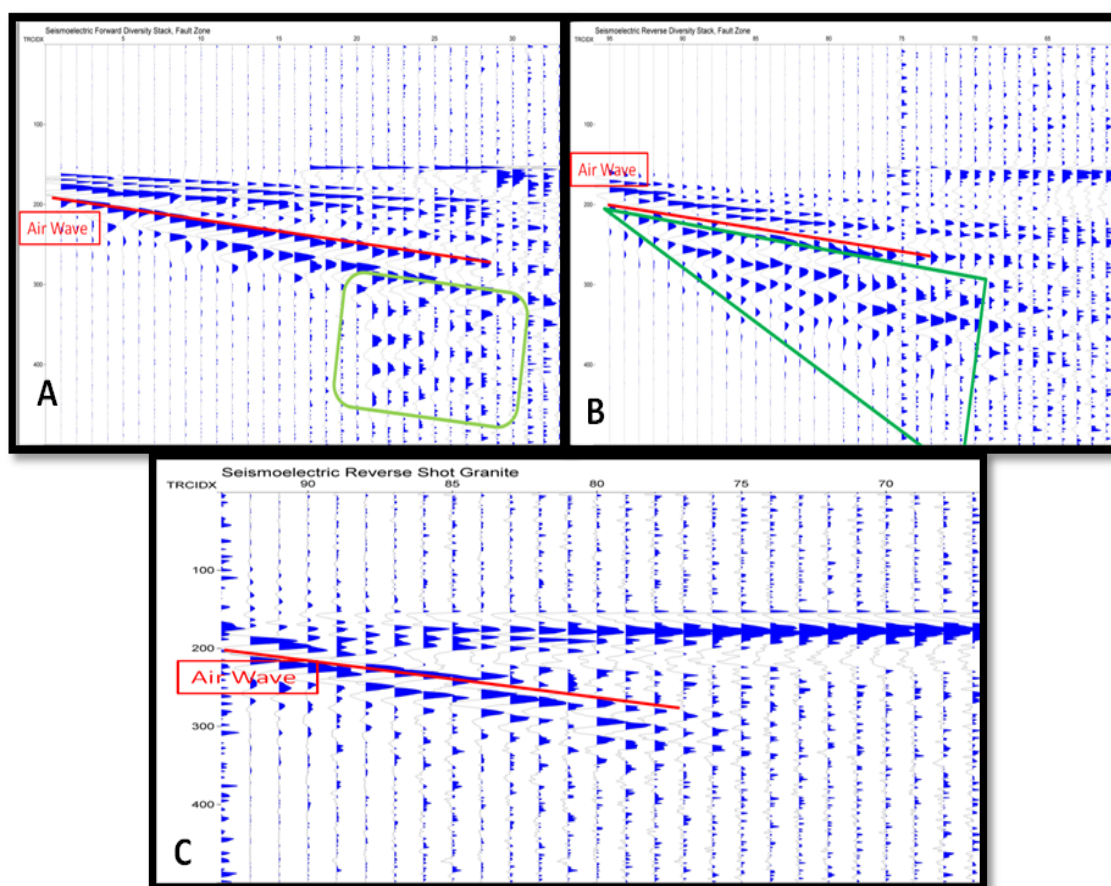


Figure 31. Seismoelectric records from Mason WMA field site; (A and B) fault zone, (C) granite area. Air waves highlighted in red. Anomalous wave energy circled in green.

CONCLUSIONS

Seismoelectric and seismic data sets from a granite/sandstone fault at the Mason WMA were collected, processed, and interpreted. Seismoelectric field measurements may reveal evidence of a guided wave trapped and transmitted through a known fault system. The hypothesis was investigated that seismoelectric fault-trapped waves indeed provide improved imaging over conventional seismic techniques. This hypothesis was not definitively disproved. It was confirmed that conventional seismic techniques are capable of recording fault guided waves. Independent analysis of the seismoelectric data showed that the seismoelectric method is also capable of imaging fault guided waves. Late-arriving energy with anomalously high amplitudes was seen in the seismoelectric records.

The seismoelectric records collected do not show as definitive results as seismic records, but there are several factors to take into account when comparing the two data sets. The fact that ordinary seismoelectric signals are much smaller in amplitude than seismic signals provides a challenge in resolving any seismoelectric data. Secondly, seismoelectric field methods and instrumentation are not as advanced as those of the seismic industry which is supported by hundreds of well-financed companies and has been researched and refined for over 100 years. A positive effect of the seismoelectric method is that ground-roll motion is not seen in the data since the electric dipoles only record vertical particle motion. Lastly, guided waves have been previously studied and modeled in seismic theory and field experiments while the seismoelectric phenomena

has not been applied to the study of fault-guided waves, theoretically or experimentally. These differences must be taken into account when comparing the two techniques.

Multiple steps might be taken in the future to refine this experiment and produce more decisive tests of the investigated hypothesis. Firstly, the seismoelectric theory should be applied to the guided-wave governing equations. Understanding the interactions of the electric double layer within a laterally multi-layered system of varying physical and chemical properties could prove useful and shed some insight into the expected field results. Numerical modeling and simulations performed with these governing equations should then be performed to understand synthetic responses. Finally, field experiments designed with this information in mind should be undertaken.

REFERENCES

- Beamish, D., and Peart, R., 1998, Electrokinetic geophysics. a review: *Terra Nova*, **10**, no. 1, 48-55.
- Ben-Zion, Y., 1998, Properties of seismic fault zone waves and their utility for imaging low-velocity structures, *Journal of Geophysical Research*, **103**, no. b6, 567-585.
- Biot, M., 1956a, Theory of propagation of elastic waves in a fluid-saturated porous solid, i. low-frequency range: *J. Acoustic. Soc. Am.*, **28**, 168-178.
- Biot, M., 1956b, Theory of propagation of elastic waves in a fluid-saturated porous solid, ii. higher-frequency range: *J. Acoustic. Soc. Am.*, **28**, 178-191.
- Butler, K. E., and Russell, R. D., 1993, Subtraction of powerline harmonics from geophysical records (short note): *Geophysics*, **58**, no. 06, 898-903.
- Butler, K. E., Russell, R. D., Kepic, A. W., and Maxwell, M., 1996, Measurement of the seismoelectric response from a shallow boundary: *Geophysics*, **61**, no. 06, 1769-1778.
- Gorham, J., 2010, An evaluation of a vibroseis source for acquiring seismoelectric data:, Report No.: GPH 11/10.
- Haartsen, M. W., and Pride, S. R., 1997, Electro seismic waves from point sources in layered media: *J. Geophysics. Res.*, **102**, no. B11, 24745-24769.
- Haines, S., 2004, Seismoelectric imaging of shallow targets, Stanford Exploration Project No. 119.
- Ivanov, A., 1939, Effect of electrization of earth layers by elastic waves passing through them: *Dokl. Adad. Nauk SSSR*, **24**, no. 1, 41-45.
- Kepic, A. W., Maxwell, M., and Russell, R. D., 1995, Field trials of a seismoelectric method for detecting massive sulfides, *Geophysics*, **60**, no. 02, 365-373.
- Li, Y.G., and Vidale, J., 1996, Field measurement of the electro seismic response: *Geophysics*, **40**, no. 02, 233-245.
- Long, L. T., and Rivers, W. K., 1975, Low-velocity fault zone guided waves: numerical investigations of trapping efficiency, *Bulletin of the Seismological Society of America*, **86**, No. 2, 371-378.
- Maxwell, M., Russell, R. D., Butler, K. E., and Kepic, A.W., 1992, Field tests of piezoelectric exploration for quartz: SEG 62nd Annual International Meeting, 443-445.

Mikhailoz, O. V., Haartsen, M. W., and Toksoz, M. N., 1997, Electro seismic investigation of the shallow subsurface: field measurements and numerical modeling: *J. Geophysics. Res.*, **62**, no. 01, 97-105.

Neev, J., and Yeatts, F., 1989, Electrokinetic effects in fluid-saturated poroelastic media: *Physical Review B*, **40**, no. 13, 9135-9141.

Pride, S. R., and Haartsen, M.W., 1996, Electro seismic wave properties: *J. Acoustic. Soc. Am.*, no. 3, 1301-1315.

Pride, S., 1994, Governing equations for the coupled electromagnetics and acoustics of porous media: *Physical Review B*, **50**, no. 21, 15678-15696.

Russell, R. D., Butler, K. E., Kepic, A. W., and Maxwell, M., 1997, Seismoelectric exploration: *The Leading Edge*, **16**, no. 11, 1611.-1615.

Shtivelman, V., Marco, S., Reshef, M., Agnon, A., Hamiel, Y., 2005, Using trapped waves for mapping shallow fault zones, *Near Surface Geophysics*, no. 3, 93-99.

Texas Parks and Wildlife Department, 1999, Mason Mountain WMA, www.tpwd.state.tx.us/huntwild/hunt/wma/find_a_wma/list/?id=14, accessed March 2012.

Thompson, A. H., and Gist, G. A., 1993, Geophysical applications of electrokinetic conversion: *The Leading Edge*, **12**, no. 12, 1169-1173.

Thompson, R. R., 1936, The seismic electric effect: *Geophysics*, **01**, no. 03, 327-335.

Thompson, R. R., 1939, A note on the seismic-electric effect: *Geophysics*, **04**, no. 02, 102-105.

Wu, J. and Hole, J., 2011, Refraction of fault-zone guided seismic waves: *Bulletin of the Seismological Society of America*, **101**, No. 4, 1674-1682.

Zhu, Z., Haartsen, M. W., and Toksoz, M. N., 1999, Experimental studies of electrokinetic conversions in fluid-saturated borehole models: *Geophysics*, **64**, no. 5, 1349-1356.

VITA

Frelynn Joseph Reese Cohrs

5211 Mimosa Dr.
Bellaire, TX 77401
frelynn.cohrs@gmail.com

EDUCATION

Colorado School of Mines, Golden, CO
B.S. Geophysical Engineering May 2010

Texas A&M University, College Station, TX
M.S. Geophysics May 2012

EXPERIENCE

Apache Corp.; Houston, TX Summer 2011
Modeling of elastic and acoustic synthetic seismic data (acquisition parameters and geometries)

Stone Energy Inc.; Houston, TX Summer 2010
Interpretation of seismic data and pressure volumes from deep shelf Gulf of Mexico in variety of interpretation suites for prospect characterization and technical review/presentation

Olson Engineering Inc.; Denver, CO January 2008-May 2010
Performed non-destructive geophysical investigations, maintained/customized geophysical equipment

Department of Geophysics, CSM; Buena Vista, CO Summer 2009
Processed and correlated 2-D Deep Seismic Data, 3-D Seismic Survey, Gravity, Magnetism, Electromagnetic, and Vertical Seismic Profile Data

Rock Abuse Laboratory; Golden, CO Summer 2007
Performed core sample pressure/fluid experiments and heavy oil toluene extractions